Available online at www.sciencedirect.com

ScienceDirect

Geochimica et Cosmochimica Acta 334 (2022) 14–44

Geochimica et Cosmochimica Acta

www.elsevier.com/locate/gca

Impact of submarine groundwater discharge on biogeochemistry and microbial communities in pockmarks

Lotta Purkamo [a,*], Cátia Milene Ehlert von Ahn [b], Tom Jilbert [c], Muhammad Muniruzzaman [a], Hermann W. Bange [d], Anna-Kathrina Jenner [b], Michael Ernst Böttcher [b,e,f], Joonas J. Virtasalo [g]

[a] *Water Management Solutions, Geological Survey of Finland (GTK), Vuorimiehentie 5, FI-02150 Espoo, Finland*
[b] *Geochemistry and Isotope Biogeochemistry Group, Leibniz Institute for Baltic Sea Research (IOW), Seestraße 15, D-18119 Warnemünde, Germany*
[c] *Environmental Geochemistry Group, Department of Geosciences and Geography, Gustaf Hällströmin katu 2, University of Helsinki, Finland*
[d] *Marine Biogeochemistry, GEOMAR Helmholtz Centre for Ocean Research Kiel, Düsternbrooker Weg 20, D-24105 Kiel, Germany*
[e] *Marine Geochemistry, University of Greifswald, D-17489 Greifswald, Friedrich-Ludwig-Jahn-Straße 17a, Germany*
[f] *Department of Maritime Systems, Interdisciplinary Faculty, University of Rostock, D-18059 Rostock, Albert-Einstein-Straße 21, Germany*
[g] *Marine Geology, Geological Survey of Finland (GTK), Vuorimiehentie 5, FI-02150 Espoo, Finland*

Received 7 December 2021; accepted in revised form 29 June 2022; Available online 21 July 2022

Abstract

The impact of submarine groundwater discharge (SGD) on coastal sea biogeochemistry has been demonstrated in many recent studies. However, only a few studies have integrated biogeochemical and microbiological analyses, especially at sites with pockmarks of different degrees of groundwater influence. This study investigated biogeochemical processes and microbial community structure in sediment cores from three pockmarks in Hanko, Finland, in the northern Baltic Sea. Pockmark data were supplemented by groundwater and seawater measurements. Two active pockmarks showed SGD rates of 0.02 cm d^{-1} and 0.31 cm d^{-1}, respectively, based on porewater Cl^- profiles, while a third pockmark had no SGD influence. Reactive transport modelling (RTM) established that the porewater systems of these active pockmarks are dominated by advection, resulting in the focusing of biogeochemical reactions and the microbial community into a thin zone at the sediment surface. The advection further reduces the accumulation of organic matter in the surface sediments, resulting in the absence of a sulfate-methane transition zone (SMTZ) at these pockmarks. Furthermore, the RTM estimated low rates of consumption of SO_4^{2-}, and low rates of production of CH_4, NH_4^+, DIC at the active pockmarks. Archaeal communities in the active pockmarks were dominated by ammonia-oxidizing archaea of predominantly groundwater origin. In contrast, at the inactive pockmark, the lack of SGD has permitted rapid deposition of organic-rich mud. The porewater system in the inactive pockmark is dominated by diffusion, leading to orders of magnitude higher metabolite concentrations at depth compared to the active pockmarks. The biogeochemical environment in the inactive pockmark resembles typical organic-rich mud seafloor in the area, with sulphate reduction and methanogenesis dominating organic matter remineralization. Accordingly, methanogens dominate the archaeal community, whereas sulfate reducers dominate the bacterial community. RTM results suggest that sulfate-mediated anaerobic oxidation of methane (S-AOM) also occurs at this site. Although depth-integrated fluxes of SO_4^{2-}, CH_4, NH_4, DIC at the inactive pockmark are orders of magnitude higher compared to the active pockmarks, processes at the inactive pockmark represent internal recycling in the coastal sea. Fluxes observed at the active pockmarks, although comparatively small in magnitude, are partly influenced by external inputs to the sea through SGD. Hence, effluxes across the sediment–water interface at these sites partly represent direct external fluxes to the marine environment, in addition to

* Corresponding author.
E-mail address: lotta.purkamo@gtk.fi (L. Purkamo).

https://doi.org/10.1016/j.gca.2022.06.040

diagenetic recycling at the benthic interface. The study highlights that SGD can result in significant spatial heterogeneity of biogeochemical processes and microbial community structure in the coastal zone, and that the overall effects of SGD and associated solute fluxes at an SGD site are a function of the number of pockmarks, the rate of SGD, and the ratio of active to inactive pockmarks.

Keywords: Submarine groundwater discharge; Microbial community; Reactive transport modelling; Coastal sediment; Baltic Sea

1. INTRODUCTION

Coastal aquifers are groundwater systems connecting the exchange of water and substances between land and sea, and represent specific hydrogeological characteristics that lead to submarine groundwater discharge (SGD) into marine ecosystems. SGD is commonly defined as the flow of groundwater from coastal aquifers to the sea often with a fraction of admixed recirculated seawater, and it is increasingly recognized by the scientific community as an important pathway for material transport across the land-sea interface (e.g., Church, 1996; Moore, 2010; Knee and Paytan, 2011; Moosdorf et al., 2021). The global flux of fresh SGD to the Ocean has been estimated to an equivalent of about 1% of riverine discharge (Luijendijk et al., 2020; Zhou et al., 2019) and the fluxes of N and P through fresh SGD alone to the global ocean are estimated to reach up to 10% of those derived from river discharge (Cho et al., 2018). The N and P fluxes through total SGD (fresh + recir culated seawater), however, may exceed riverine inputs on the global scale (Cho et al., 2018), and can substantially impact coastal ecosystems and water quality on regional and local scales (Johannes, 1980; Bernard et al., 2014; Oehler et al., 2021; Santos et al., 2021; Böttcher et al., 2020). SGD may have implications on the production of dissolved and gaseous metabolites, such as NH_4^+, DIC, CH_4, and H_2S (e.g., Schlüter et al., 2004; Idczak et al., 2020; O'Reilly et al., 2021). One of the challenging ongoing questions is the representativity of groundwater observation wells for the freshwater component reaching the mixing zone with sea water (e.g., Beck et al., 2007; von Ahn et al., 2021), and another one, the role of diagenetic processes in marine sediments covering the aquifers for the modulation of the fluid composition finally being released to the coastal waters (e.g., Donis et al., 2017).

SGD can occur at sites close to the shoreline or further offshore, and the internal structure and uneven permeability distribution in aquifers can result in focusing of the groundwater discharge, leading to the development of local depressions (pockmarks) on the seafloor as observed by Jensen et al. (2002), Virtasalo et al. (2019) and Hoffmann et al. (2020). Physical and chemical gradients in pockmarks induced by SGD add to the heterogeneity of the seafloor because they provide distinct biogeochemical environments with specific active biological communities and microbial metabolisms compared with the surrounding seafloor (Kotwicki et al., 2014; Lecher and Mackey, 2018 and references within). For example, changes in salinity have been shown to affect the composition of seafloor microbial community structure and biogeochemical activity (Santoro et al., 2008; Lee et al., 2017; Klier et al., 2018; Donis et al., 2017; Adyasari et al. 2019). SGD can also affect the benthic community through a significant reduction in the meiofaunal density (Kotwicki et al. 2014).

In the Baltic Sea, the presence of pockmarks associated with SGD has been described in a several areas mostly restricted in the southern part: Eckernförde Bay in Germany (e.g., Whiticar and Werner, 1981; Schlüter et al., 2004; Hoffmann et al., 2020), the Laholm Bay in Sweden (Vanek and Lee, 1991), and Gulf of Gdansk in Poland (Idczak et al., 2020). A recent study in the northern Baltic Sea, in Hanko (Finland), documented a distinct SGD release for up to 20 pockmarks on the sandy shore platform slope at water depth between 4 and 17 m (Virtasalo et al., 2019). The geological structure of the silicate rock aquifer, and groundwater flow pathways to the pockmark area, were successfully modelled by Luoma et al. (2021). However, studies relating SGD and the microbial community composition remain scarce in the Baltic Sea (Idczak et al. 2020), as well as in coastal sea areas in general (Haverkamp et al. 2014; Adyasari et al. 2019, 2020).

The present study investigates the biogeochemical processes and microbial community structure in seafloor pockmarks at the Hanko SGD site in the northern Baltic Sea (Virtasalo et al., 2019; Fig. 1). The major aims were to quantify SGD and associated material fluxes from individual pockmarks to gain understanding about the impacts of salinity, SGD rate and organic matter availability on the microbial ecology and production of organic metabolites of ecosystem importance.

2. STUDY AREA

The Hanko SGD site is located in Lappohja, on the southeastern side of the Hanko cape on the south coast of Finland. The location is characterized by an arc-shaped sandy beach, a sandy shore platform that extends 100–250 m seaward sloping gently to ca. 4 m water depth, and a steep slope to ca. 17 m water depth within ca. 50 m distance (Fig. 1). The SGD takes place predominantly through pockmarks, which are up to 25 m wide and 2 m deep depressions on the edge and slope of the shore platform. Approximately twenty pockmarks have been identified at the site, but only three larger ones have been studied in detail: B, D and E (Fig. 1). Elevated ^{222}Rn activities 1 m above pockmarks B and D in May 2018 indicate fresh groundwater discharge rates of 0.40 – 1.22 cm d^{-1} (Virtasalo et al., 2019). Pockmark E was found to be covered by a soft mud layer, and did not show ^{222}Rn activity above background values, which indicates that it is cur-

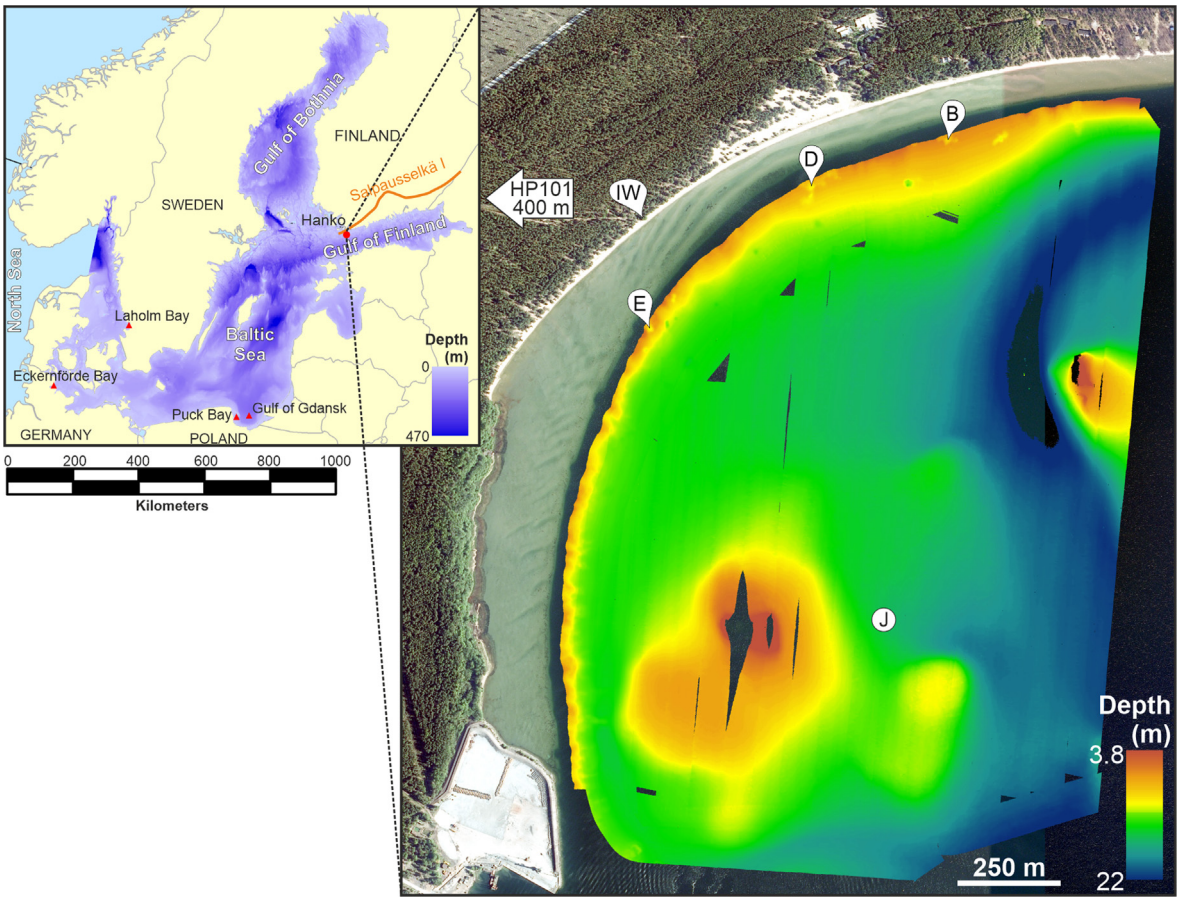

Fig. 1. Multibeam bathymetric image over the study area. The locations of pockmarks B, D and E, offshore seawater reference station J, and the obsolete water intake well (IW) are indicated. Groundwater observation well HP101 is located ca. 400 m west from the upper left side of the image. Red dot in the inset indicates the Hanko SGD site studied here. Red triangles indicate other documented SGD sites in the Baltic Sea region (Vanek and Lee, 1991; Schlüter et al., 2004; Szymczycha et al., 2012; Idczak et al., 2020). Aerial photograph: National Land Survey of Finland Topographic Database 04/2017. Baltic Sea bathymetric map: EMODnet Bathymetry DTM 2020. Modified from Virtasalo et al. (2019). (For interpretation of the references to colour in this figure legend, the reader is referred to the web version of this article.)

rently inactive. Comparable fresh groundwater discharge rates between 1.2 and 1.6 cm d^{-1} were estimated by a transient groundwater flow model for the same date (Luoma et al., 2021).

The shore platform and pockmarks are located in the distal part of ice-contact fan deposits that belong to the First Salpausselkä ice-marginal formation (Virtasalo et al., 2019), which is an extensive and narrow ridge that is composed of sand and gravel, with till beds particularly on its northwestern (ice-proximal) side (Fyfe, 1990; Kujansuu et al., 1993). The ridge was deposited in front of the Fennoscandian continental ice-sheet, in an ice-contact lake that was >100 m deep in Hanko (Fyfe, 1990), by 12,100 varve years before the year 2000, when the retreat of the ice margin came to a halt for ca. 217 years during the Younger Dryas climatic cooling (Sauramo, 1923; Saarnisto and Saarinen, 2001). The sediments rest on the Paleoproterozoic crystalline bedrock that mainly consists of quartz diorite and granodiorite (Kielosto et al., 1996). As a result of initially rapid glacio-isostatic land uplift (today 4 mm yr^{-1}; Kakkuri, 2012), the First Salpausselkä ridge has emerged above sea level. The top of the ice-marginal formation was exposed to waves and eventually to wind as it gradually rose from the sea, and the original ridge morphology became truncated and flattened from the top (Fyfe, 1990).

The Hanko area belongs to the humid continental climate type with cold, wet winters, and to the mixed-coniferous forest zone. The mean annual air temperature is 6.0 °C, with the mean minimum air temperature of 3.3 °C and the mean maximum air temperature of 8.8 °C. The mean annual precipitation is 634 mm during the period 1981–2010 (Pirinen et al., 2012). The annual mean sea surface salinity ranges between 4.5 and 6.5 and the annual mean sea surface temperature ranged between 4 and 9 °C during the period 1927–2011 (Merkouriadi and Leppäranta, 2014). The low salinity results from the high riverine runoff from the large Baltic Sea catchment area, and from the long distance to the narrow connection to the North Sea through the Danish straits. The sea is annually covered by ice on average 69 days (1891–2012), and the ice season usually ends in April (Merkouriadi and Leppäranta, 2014). The sea is essentially non-tidal, but irregular water level fluctuations of as much as 2.1 m take

place as a result of variations in wind and atmospheric pressure (Wolski et al., 2014).

3. MATERIALS & METHODS

3.1. Sample collection

Seawater, sediment and porewater samples were collected on 26–27th of September 2019 (Table 1) at pockmarks B, D and E onboard the R.V. Geomari of the Geological Survey of Finland (GTK).

Seawater samples were collected using a Limnos water sampler at three depths: surface water 2 m below sea surface, mid-water 6 m below sea surface, and bottom water 1 m above the pockmark bottom. In addition, a surface water sample was collected from the offshore reference station J. Samples for methane analyses were poured into triplicate 20 mL glass vials that were sealed with rubber caps avoiding air bubbles and preserved by adding 50 μL of $HgCl_2$(aq) (0.7 g $HgCl_2$ dissolved in 10 mL water) through the caps using a needle. Samples for dissolved ammonium (NH_4^+) were filtered through 0.45 μm cellulose acetate disposable membrane filters (Carl Roth, Karlsruhe, Germany) in pre-rinsed 20 mL PE vials and kept frozen until analysis. For microbiological analyses, bottom water samples above pockmarks and a control seawater sample from offshore station (two replicate samples from each, marked a and b) were poured into 500 mL acid-cleaned and autoclaved glass bottles (Schott), closed and stored in cool and dark until analysis.

Sediment cores from the pockmarks B and D with the penetration of 5 and 11 cm, respectively, were collected using a box corer (18 × 18 × 25 cm), because the stiff fine sand composition of the pockmark bottom prevented sufficient penetration by a Gemax corer. The box corer had an internal removable plastic liner, which captured the near-bottom water and sediment with an undisturbed surface. The water was carefully removed prior to the removal of the plastic liner in order to preserve the sediment core intact. Porewater salinity was measured using a hand refractometer (ATAGO) with a precision of 1 ‰. Samples for methane, multielement, Cl^-, NH_4^+, DIC and $\delta^{13}C_{DIC}$ analyses were extracted by pushing separate sets of rhizons (Rhizosphere Research Products, Wageningen, The Netherlands) to the side of the core at 1 cm intervals in a zig-zag pattern for the entire core length. For multielement and Cl^- analyses, 10 mL of porewater was transferred from the Rhizon syringes to 15 mL polyethylene tubes at each depth. No preservatives were added to the samples because the multielement and Cl^- analyses commenced within a few days. For methane analysis, 2 mL of porewater was collected in the rhizon syringe under vacuum. 8 mL of nitrogen gas (N_2, purity 5.0) was injected into the syringe via a 3-way tap, and the water–gas mixture was allowed to reach ambient temperature (25 °C), before being equilibrated by shaking for 5 mins. 5 mL of headspace gas was then extracted via a 3-way tap into a dry syringe and subsequently into a pre-evacuated 3 mL Exetainer® vial with double-wadded septum for storage (Labco ltd., Lampeter, Ceredigion, United Kingdom). Samples for DIC and $\delta^{13}C_{DIC}$ were filled without headspace into 3 mL Exetainer® tubes (Labco ltd., Lampeter, Ceredigion, United Kingdom), previously cleaned with 2% HNO_3 and pre-filled with 25 μL $HgCl_2$. All porewater samples were sealed and stored in cool and dark until analysis. For NH_4^+, 2 mL of porewater were transferred into pre-rinsed Eppendorf plastic vials and kept frozen until analysis. A sediment core from the pockmark E was collected using a Gemax twin-barrel short gravity corer (internal diameter 9 cm), which penetrated 54 cm into the soft mud, preserving the sediment surface intact. Porewater samples were collected by separate sets of Rhizons, pushed into the sediment and overlying water at 2 cm intervals through pre-drilled holes on the side of the core liner. Further processing of these samples was identical to those from the box cores described above.

After porewater extraction, the box-cores were sliced using a knife at 1 cm vertical intervals for multielement composition analysis and at 1.5–2.5 cm and 3.5–4.5 cm depths for microbial community analyses. Sedimentologic structure of the cores was inspected during the slicing. The Gemax core of pockmark E was cut in 1 cm sample slices using a rotary device. The twin of the pockmark E Gemax-core was split lengthwise for sedimentological inspection. Sediment samples were sealed and stored in cool and dark prior to analysis. Sediment subsamples (two replicates from each, marked a and b) for molecular microbiology community analysis were frozen in dry ice in the field and kept at −20 °C until further analysis.

Groundwater samples of the observation well HP101 and an obsolete water intake well near the shoreline were collected on 28th of September 2019 (Table 1). Prior to sampling, the waters were measured for temperature, electrical conductivity, pH, dissolved oxygen and redox potential using a WTW Multiline *P*4 meter (WTW GmbH, Weilheim, Germany). Observation well HP101 was sampled using a suction pump and allowing the pumped water to

Table 1
Sampling sites, and the types and dates of samples collected.

	Latitude N (WGS84)	Longitude E (WGS84)	Water samples	Porewater samples	Sediment samples
Pockmark B, active	59°53.771′	23°14.478′	26 September 2019	26 September 2019	26 September 2019
Pockmark D, active	59°53.700′	23°14.129′	26 September 2019	26 September 2019	26 September 2019
Pockmark E, inactive	59°53.501′	23°13.732′	27 September 2019	27 September 2019	27 September 2019
Offshore station J, seawater reference	59°53.164′	23°14.367′	27 September 2019		
Groundwater, observation well HP101	59°53.616′	23°12.674′	28 September 2019		
Groundwater, obsolete water intake well	59°53.660′	23°13.688′	28 September 2019		

run for several minutes until the measured parameters reached stable values in order to obtain fresh samples. Groundwater level was measured at 4.36 m, and the base of the pump filter was lowered to ca. 8.5 m below the top of the well steel surface casing. The obsolete water intake well was sampled by collecting water that was gently leaking from its wall. Samples for multielement and Cl^- analyses were collected in 100 mL polyethylene bottles with no preservatives added. Groundwater and water column samples for methane analyses were collected into triplicate 20 mL glass vials that were sealed with rubber caps avoiding air bubbles and preserved by adding 50 µL of $HgCl_2$(aq) solution through the caps using a needle. Samples for DIC and $\delta^{13}C_{DIC}$ were filled without headspace into 3 mL Exetainer® tubes (LABCO ltd., Lampeter, Ceredigion, United Kingdom), previously cleaned with HNO_3, washed, dried and filled with 25 µL saturated $HgCl_2$ solution. Samples for microbiological analyses were collected into duplicate 1000 mL acid-washed and autoclaved Schott bottles. All water samples were sealed and stored in cool and dark until analysis. For NH_4^+ analysis, 15 mL of porewater were transferred into pre-rinsed 20 mL polyethylene bottles and kept frozen until analysis.

3.2. Analytical methods

3.2.1. Analysis of water samples

Groundwater, seawater and porewater samples were analyzed at the accredited laboratory Eurofins Labtium Ltd in Espoo, Finland. Alkalinity (as HCO_3^-), electrical conductivity, pH and $KMnO_4$ consumption of the unfiltered and unpreserved groundwater samples were measured immediately upon arrival at the laboratory. Multielement composition of seawater, groundwater and porewater samples were analyzed using inductively coupled plasma optical emission and mass spectrometry (ICP-OES and ICP-MS). Ca, Fe, K, Li, Mg, Mn, Na, and S were analyzed by ICP-OES (method SFS-EN ISO 11885) using a Thermo Scientific iCAP 7600 Duo Spectrometer, whereas Ag, Al, As, B, Ba, Be, Bi, Cd, Co, Cr, Cu, I, Li, Mn, Mo, Ni, P, Pb, Rb, Sb, Se, Sr, Th, Tl, U, V, and Zn were analyzed by ICP-MS (SFS-EN ISO 17294-2) using a ThermoScientific iCAP Q spectrometer (Thermo Fisher Scientific Inc., Waltham, Massachusetts, USA). In all water samples, the measured S is considered to consist essentially of SO_4^{2-}. Chloride was analyzed with ion chromatography (SFS-EN ISO10304-1) using a Dionex ICS-2000 system (Dionex Co., Sunnyvale, California, USA). To check the quality of the analysis, blind duplicate samples were included in the analysis batch.

For methane analysis of porewaters, helium (He) was injected into the Exetainer® vials to achieve a pressure of 2.0 bar prior to autoinjection into the gas chromatograph (Agilent technologies 7890B custom, equipped with flame ionization detector (FID), electron capture detector (ECD) and thermal conductivity detector (TCD), and He used as carrier gas). Methane (CH_4) mole fractions were determined by FID. Simultaneous measurement of N_2 and O_2 + Ar (TCD) allowed a 100% sum to be calculated for estimation of normalized CH_4 mole fractions in the unpressurized headspace sample. Temporal drifts of CH_4 signals due to detector sensitivity were accounted for by analyzing standard gas samples at 12-sample intervals (Penttilä et al., 2013). Headspace CH_4 mole fractions were converted to total dissolved CH_4 concentrations in the original porewater sample (C_{tot} in equation (1)) using Henry's Law (Myllykangas et al., 2017). The first term on the right side represents the contribution to C_{tot} of dissolved gas released into the headspace during equilibration, while the second term represents the contribution from gas remaining in the dissolved phase:

$$C_{tot} = (X_{HS} \cdot P_{atm} \cdot V_{HS})/(R \cdot T \cdot V_{aq}) + F \cdot X_{HS} \cdot P_{atm} \quad (1)$$

where X_{HS} is the mole fraction of the CH_4 in the headspace in ppm, P_{atm} is the pressure in the headspace in atm (set to 1 atm), V_{HS} and V_{aq} are the headspace and water volume in mL respectively, R is the gas constant (0.08206 L atm/K mol^{-1}), T the temperature in Kelvin during equilibration (293 K), and F is the temperature/salinity-dependent equilibrium solubility coefficient of CH_4 in mol/L atm^{-1}, as detailed in Wiesenburg and Guinasso (1979).

Groundwater and seawater column samples were analyzed for methane at GEOMAR Helmholtz Centre for Ocean Research Kiel, Germany, within a few weeks after sampling. For the determination of CH_4 concentrations, the static-headspace equilibration method was applied, followed by gas chromatographic separation and detection with a FID as described in Bange et al. (2010). Calibration of the FID was performed with standard gas mixtures of 1806.10 – 3003.79 ppb CH_4 in synthetic air, which have been calibrated against NOAA-certified primary gas standards in the laboratory of the Max Planck Institute for Biogeochemistry in Jena, Germany. Final dissolved CH_4 concentrations (C_{tot}) were calculated according to equation (1).

$\delta^{13}C_{DIC}$ values were determined as described by Winde et al. (2014) by means of isotope-ratio-monitoring mass spectrometry (irmMS) using a Thermo Finnigan MAT253 gas mass spectrometer attached to a Thermo Electron Gas Bench II via a Thermo Electron Conflo IV split interface. Solutions were allowed to react for at least 18 h at room temperature before introduction into the mass spectrometer. International and in-house standards were used for calibration of measured isotope ratios towards the V-PDB scale. Throughout the paper, isotope ratios are expressed in mUr that equals the traditional ‰ in the ∂-notation (Brand and Coplen, 2012).

The concentrations of NH_4^+ were analyzed spectrophotometrically based on Berthelot reaction following Grasshoff et al. (2009) on a QuAAtro autoanalyzer system (Seal Analytical, Southampton, UK).

3.2.2. Analysis of sediment samples

Sediment samples were analyzed for ^{137}Cs activity content to constrain sedimentation rate in each core. The ^{137}Cs activity of untreated samples was measured for 60 min, using a BrightSpec bMCA-USB pulse height analyser coupled to a well-type NaI(Tl) detector at the GTK (Ojala et al., 2017). No corrections were applied for the results because the aim was only to detect relative ^{137}Cs

activity peaks. Due to the possible post-depositional downward transport of ^{137}Cs through bioturbation and diffusion (Holby and Evans, 1996; Klaminder et al., 2012), the depth of peak ^{137}Cs activity (rather than the initial increase) was assumed to represent the fallout from the 1986 Chernobyl nuclear disaster.

After the non-destructive ^{137}Cs analysis, sediment samples were freeze-dried, homogenized and halved, with one half analyzed for multielement composition and the other for grain size distribution at the laboratory (Eurofins Labtium ltd, Kuopio, Finland). The material for multielement analysis was sieved through a 63 μm mesh, and 0.2 g of the passed-through fraction was digested in a four-acid mixture of hydrofluoric acid, perchloric acid, hydrochloric acid and nitric acid (USGS Methods T01 and T20). After evaporation of the acids at 160 °C, the resulting gel was dissolved in 1 M HNO_3, and analyzed for element concentrations. Al, Ba, Be, Ca, Cr, Cu, Fe, K, Li, Mg, Mn, Mo, Na, Ni, P, Pb, S, Sc, Sr, Ti, V, Y, Zn, and Zr were analyzed by ICP-OES using Ta Thermo Scientific iCAP 6500 Duo spectrometer, whereas Ag, As, Bi, Cd, Ce, Co, Dy, Er, Eu, Gd, Hf, Ho, La, Lu, Nb, Nd, Pr, Rb, Sb, Sm, Sn, Ta, Tb, Th, Tl, Tm, U, and Yb were analyzed by ICP-MS using a Thermo Scientific iCAP Qc spectrometer (Thermo Fisher Scientific, Inc., Waltham, Massachusetts, USA). Because HF dissolves silicate minerals, the digestion is considered as "near-total digestion" (Hall et al., 1996). The commercial sediment reference materials QCGBMS304-6, QCMESS-4, QCNIST8704, CO153B and in-house standards were used for assessing measurement accuracy. Element concentrations for all reference materials measured with each sample batch fell well within ± 10% of the certified values. Mercury was measured separately for 0.2 g samples through thermal decomposition, amalgamation and atomic absorption spectrometry (US EPA Method 7473) using an Altec AMA254 Hg-analyzer (Altec, Prague, Czech Republic). Solid-phase contents of carbon and nitrogen in the samples were analyzed by thermal combustion elemental analysis (TCEA) using an Elementar vario MAX Cube elemental analyzer (Elementar Analysensysteme GmbH, Langensebold, Germany). Total inorganic carbon (TIC) was analyzed using a Thermo Finnigan MAT 253 gas mass spectrometer coupled with a Thermo Electron Gas Bench II via a Thermo Electron Conflo IV split interface (Schaller et al., 2022). Solid $CaCo_3$, Li_2CO_3, and liquid $NaHCO_3$ standards were used to scale the mass 44 measurements to TIC contents (Supplementary Material, Table S1).

The sediment grain size distribution was measured on freeze-dried samples by wet-sieving through 20 mm, 6.3 mm, 2 mm, 0.63 mm, 0.2 mm and 0.063 mm ISO 3110/1 test sieves. The samples were pretreated with excess H_2O_2 to remove organic matter prior to the analysis. The < 63 μm size fraction was further analyzed down to 0.6 μm using a Micromeritics Sedigraph III 5120 X-ray absorption sedimentation analyzer (Micromeritics Co., Norcross, Georgia, USA). The granulometric results were merged with sedimentation data in Sedigraph software. Median grain size was calculated according to the geometric Folk and Ward (1957) graphical measures, as implemented in the Rysgran 2.1.0 package in the R 4.0.2 software environment. The clay fraction is defined here as grain sizes smaller than 2 μm, whereas mud is composed of the clay and silt (<63 μm) fractions, and sand is defined by grain sizes between 63 μm to 2 mm (Blott and Pye, 2012).

3.2.3. Biomass collection and DNA extraction

Biomass was collected from water samples by filtering in a laminar flow hood. Filters were frozen to −20 °C prior to DNA extraction. Groundwater samples (1500 mL) were filtered through 0.1 μm PES filters (Corning Inc., Corning, NY, USA), and seawater samples (500 mL) were filtered first through 0.2 μm CA filters (Corning Inc., Corning, NY, USA) and flow through from parallel samples was pooled and further filtered through 0.1 μm PES filter. Filter paper was cut out of the funnel and placed into a sterile 50 mL plastic tube and frozen prior to further processing. DNA was extracted with DNeasy PowerWater kit (Qiagen, Hilden, Germany) according to the manufacturer's protocol, starting from step 5. DNA was eluted with 100 μL of EB buffer provided by the kit.

DNA extraction for sediment samples was done directly using DNEasy Powersoil Pro Kit (Qiagen, Hilden, Germany). Sediment samples were thawed, and 250 mg of each sample was weighed to bead tubes provided by the extraction kit. DNA was extracted according to the kit manufacturer's instructions and elution was done with 100 μL of the kit's C6 solution.

DNA concentrations of the samples were measured with Qubit 2.0 Fluorometer (Invitrogen by Life Technologies, Carlsbad, CA, USA) using Qubit dsDNA HS reagent and Buffer solutions according to the manufacturer's protocol.

3.2.4. Sequencing and data analysis

Sequencing of the 16S rRNA gene region V3-V4 of bacteria was done using f357F- 5′-TACGGGAGGCAGCAG-3′ and 800R- 5′-CCAGGGTATCTAATCC-3′ primers (Turner et al., 1999; Kisand et al., 2002, respectively) and archaeal 16S rRNA gene region V3-V6 was sequenced with 340F- 5′-CCCTAYGGGGYGCASCAG-3′ and 1000R5′-GAGARGWRGTGCATGGCC-3′ primers (Gantner et al., 2011) in Eurofins Genomics (Konstanz, Germany). Sequencing was performed with Illumina MiSeq 300x300 paired-end read protocol. Sequences were processed according to MOTHUR's (v. 1.43.0) MiSeq SOP with a phylotype-based approach, omitting the mock community analysis and using default settings if not otherwise stated (Kozich et al., 2013). Bacterial sequences were quality checked and screened with make.contigs command following screen.seqs using the following parameters: maxambig = 0, maxlength = 475, and archaeal sequences maxambig = 4, maxlength = 468. *Escherichia coli* J01859.1 (for bacteria) or *Methanobacterium paludis* NC_015574.1 (for archaea) 16S rRNA gene sequence was used to reveal the exact start and end position of the sequences in the alignment. Using those as parameters for the region of interest, pcr.seqs command was used to shrink the reference alignment. One difference per 100 bases was allowed in preclustering, thus diffs = 4 for both bacteria and archaea (with average sequence length of 415 and

432, respectively) were chosen. Chimeric sequences were identified and removed, and sequences classified using Silva_nr v.138 taxonomy. Sequences classified as Chloroplasts, Mitochondria, unknown and Archaea or Bacteria (from bacterial or archaeal sequencing data, respectively) were removed from the dataset using remove.lineage command. Sequences were assigned to OTUs using phylotype method as described in MOTHUR's MiSeq SOP. Data was standardized according to the lowest number of sequences in the samples (bacteria: 44310, archaea: 2631). Rarefaction, and different diversity, coverage and richness estimates were calculated using parameters calc = nseqs-coverage-sobs-shannon-npshannon-invsimpson-chao-ace in MOTHUR. A biom.file for both archaeal and bacterial communities was constructed and used in RStudio v. 3.6.3 for visualization of the data using e.g., biomformat, ggplot2, ggpubr and ggsci packages. Statistical analyses for microbial communities and selected environmental variables were done in PAST 3.04 (Hammer et al., 2001). Principal coordinates analysis from Hellinger-transformed relative abundance data of archaeal and bacterial communities was done using Bray-Curtis and Jaccard similarity indices.

3.2.5. Quantification of ribosomal RNA gene copy numbers of bacteria and archaea and microbes potentially involved in N and C cycling and sulfate reduction

The enumeration of the 16S rRNA gene copies was done with quantitative PCR and results were used as a proxy for the total number of bacteria or archaea in samples. Quantification of nitrate reduction potential of the microbes was made using *narG* and ammonia oxidation with *amo*A marker genes. The methanotrophic community was quantified using qPCR assay based on *pmo*A gene and the potentially methanogenic community was quantified using *mcr*A gene. Putative sulfate reducers were quantified using *dsrB* marker gene. BioLine SensiFAST SYBR® No-ROX 5X mastermix (Meridian Life Science, Inc., Memphis, TN, USA) was used for mastermix preparation with 1 ul of template DNA in a single reaction. All samples were analyzed in triplicate reactions. Analyses were performed in LightCycler® 480 Instrument (Roche Diagnostics Corp., Indianapolis, IN, USA). A melting curve analysis was done after the amplification protocol to reveal any unspecific amplification. Melting curve analysis consisted of 95 °C for 10 s, 65 °C for 1 min, ramping to 95 °C with 0,11 °C/s and 5 acquisitions per °C. The program ended with cooling the reactions to 40 °C. Details for each qPCR assay are shown in Supplementary Material (Table S2).

3.3. Reactive transport modeling

The measurements performed at different pockmarks are quantitatively interpreted by means of multicomponent reactive transport modeling and by adopting a transient diagenetic model described in earlier studies (e.g., Reed et al., 2011a,b; Rooze et al., 2016; Egger et al., 2016a). This allows obtaining a better understanding of the diagenetic and burial processes from a mechanistic perspective as well as investigating the impact of individual mechanisms on the overall behavior within a coupled system. The model includes the cycling of a wide range of dissolved solutes and particulate sediment species by explicitly taking into account the advective transport both in the aqueous and solid phases, molecular diffusion in the pore water, bioturbation in the solid phase, and a suite of inter- and intra-phase biogeochemical reactions (e.g., Wang and Van Cappellen, 1996; Boudreau 1997). In all pockmarks, the modeling is performed along a 1-D sediment column, which is representative of the upper sediment layer below the seafloor.

3.3.1. Equations for multicomponent transport in sediment and porewater

The governing mass balance equations describing multicomponent reactive transport of solutes and solids in sediments can be described as,

$$\phi \frac{\partial C_{w,i}}{\partial t} = -\phi u \frac{\partial C_{w,i}}{\partial x} + \phi (D_i + D_b) \frac{\partial^2 C_{w,i}}{\partial x^2} + \sum_{r=1}^{N_r} \upsilon_{ir} R_r \quad (2)$$

$$(1-\phi) \frac{\partial C_{s,j}}{\partial t} = -(1-\phi) v \frac{\partial C_{s,j}}{\partial x} + (1-\phi) D_b \frac{\partial^2 C_{s,j}}{\partial x^2} + \sum_{r=1}^{N_r} \upsilon_{jr} R_r \quad (3)$$

where $C_{w,i}$ [ML^{-3}] and $C_{s,j}$ [ML^{-3}] represent the concentrations of i-th aqueous and j-th solid species, respectively, ϕ [-] is the porosity, D_i [L^2T^{-1}] denotes the diffusion/dispersion coefficient of the dissolved species, i in porewater, D_b [L^2T^{-1}] is the bioturbation coefficient (also known as biodiffusion coefficient) representing random small-scale displacements of solute and solid species by benthic fauna (e.g., Boudreau, 1987), x [L] is the distance from the sediment–water interface, and t [T] is the time. u [LT^{-1}] and v [LT^{-1}] represent the advective velocities of the aqueous and solid phase constituents, respectively, whereas the last quantities in the above equations denote the net reactive source/sink term with υ_{ir}[-],υ_{jr}[-] being the stoichiometric coefficient for species i and j, respectively, for the r-th reaction and R_r [$ML^{-3}T^{-1}$] being the reaction rate for r-th reaction.

In the simulations presented in this study, the porosity was considered to be depth-dependent to take into account the effects of sediment compaction (e.g., Meysman et al., 2005). In fact, the spatially-variable pattern of porosity was clearly evident in the observed profiles for all three pockmarks. We adopt the following function, which also has been utilized in numerous earlier studies focusing on submarine systems (e.g., Reed et al., 2011a,b; Egger et al., 2016a; Rooze et al., 2016):

$$\phi(x) = \phi_\infty + (\phi_0 - \phi_\infty) \exp\left(-\frac{x}{\zeta}\right) \quad (4)$$

where ϕ_0[-] is the porosity at the sediment–water interface (SWI), ϕ_∞[-] is the asymptotic porosity value at deeper depths in the sediment, and ζ [L] denotes the porosity attenuation factor or the so-called e-folding distance. The value of ζ was obtained by fitting Eq. (4) against the porosity profiles measured at different pockmarks as illustrated in the Supplementary Material (Fig. S5).

Due to a spatially variable description of porosity, both the advective velocity and the effective diffusion coefficient

also become depth-dependent quantities in the reactive transport model. In the simulations presented in the following sections, the diffusion coefficients for the dissolved and particulate chemical species were parameterized according the following relationships:

$$D_i = \frac{D_{aq,i}}{\tau} = \frac{D_{aq,i}}{1 - 2\ln(\phi)} \quad (5)$$

$$D_b(x) = D_{b0} \exp\left(-\frac{x}{\xi}\right) \quad (6)$$

where Eq. (5) represents a correction of the aqueous diffusion coefficient $D_{aq,i}$ [L^2T^{-1}] for the tortuosity (τ [-]) in porous media (Boudreau, 1996), and Eq. (6) describes the variation of the bioturbation coefficient (also termed as biodiffusion coefficient), D_b along the sediment depth with D_{b0} [L^2T^{-1}] and ξ [L] being the biodiffusion coefficient at the sediment–water interface and the mixed layer depth, respectively. The latter implies that the intensity of biogenic mixing follows an exponential decrease with depth due to the decline in faunal density with increasing depth into the sediment (e.g., Rooze et al., 2016). For simplicity, the diffusive fluxes of the dissolved/solid species are modeled with a simple Fickian formulation although the charge-induced Coulombic interactions can also exert additional controls on the transport of dissolved charged solutes (e.g., Boudreau et al., 2004; Giambalvo et al., 2002; Rolle et al., 2013; Muniruzzaman et al., 2014; Muniruzzaman and Rolle, 2015, 2017).

Furthermore, the advective velocity in the aqueous phase was estimated by optimizing the chloride concentration profiles against the analytical solution of the advection–dispersion equation under the steady-state condition. The optimization was performed as a non-linear least square method and the detailed implementation scheme is reported in the Supplementary Material. The advective velocity obtained for the different pockmarks was directly fed into the reactive transport simulations as parameter u [LT^{-1}] in Eq. (3). In contrast, the advection of the solid phase components were determined by constraining the reactive transport numerical model against the measured sediment profiles. The ^{137}Cs activity measurements provide an initial basis for the sedimentation rate for pockmark E, but further adjustment was needed in the reactive transport model to explain the observed profiles. The detailed list of the input parameters describing the flow and transport processes are reported in the Supplementary Material (Table S4, S5, S6).

3.3.2. Chemical reaction network

The transported species in the water and solid phases are tightly coupled via a wide range of biogeochemical reactions. The reaction network considered in the reactive transport simulations includes a total of 32 chemical reactions, which can be categorized into two main groups: a) primary redox reactions, and b) other biogeochemical reactions. Table 2 lists the complete set of chemical reactions incorporated in the model, and their stoichiometry as well as rate expressions were compiled from Reed et al. (2011a,b), Rooze et al. (2016) and Egger et al. (2016a). The primary redox reactions mainly include the degradation of organic matter (OM) through a variety of respiratory reactions involving O_2, NO_3^-, MnO_2, $Fe(OH)_3$ and SO_4^{2-} as terminal electron acceptors. The successive consumption of these oxidants during organic matter decomposition is typically described by Monod kinetics, which ensures the preferential use of the oxidant with the highest free energy yield followed by a sequential use of the oxidant with the next highest energy yield (Froelich et al., 1979; Berg et al., 2003; Wang and van Cappellen, 1996; Boudreau, 1996). Once these electron acceptors are exhausted, organic matter decomposition occurs via methanogenesis, where OM acts as both the electron acceptor and donor. For sulfate reduction and methanogenesis reactions, an attenuation factor, (Table S7, Supplementary Material), is considered to reproduce the slower progress of organic matter degradation during these mechanisms compared to the reactions driven by other oxidants (e.g. Moodley et al., 2005; Reed et al., 2011a, b).

The effects of distinct crystallinity and reactivity of organic matter, Mn oxides and Fe oxides were considered by assuming three different pools, representing highly reactive (α), less reactive (β) and nonreactive (γ) phases (e.g., Jørgensen, 1978; Westrich and Berner, 1984; Middelburg, 1989). In all simulations, a C:N:P ratio of 106:16:1 was used for all three organic matter pools for simplicity and it was sufficient to consistently explain the measured profiles. For Fe and Mn oxides, only the α phase was assumed to participate in OM degradation, whereas the β phase is mainly involved in the oxidation of Fe^{2+}, sulfides and methane (Table 2). In fact, this conceptualization of different reactivity for these solid species was particularly needed in order to allow the persistence of iron oxy(hydroxi)des and MnO_2 phases at deeper sediment depths (i.e., coexistence of these electron acceptors with OM) as observed in the pockmark sediment profiles.

The secondary biogeochemical reactions as listed in Table 2 describe various mineral precipitation/dissolution reactions, reoxidation of reduced metabolites, and a suite of homogeneous and heterogeneous chemical reactions. In particular, the oxidation of CH_4 is an important mechanism in this system and will be discussed in the following sections. All these secondary chemical reactions (R8 - *R*32) were simulated by considering a bimolecular rate law with the exception of a few cases where the reaction was assumed to follow a first order law (R21, R25-R28). The rate expressions for all these reactions along with the kinetic parameters used in the model are summarized in the Supplementary Material (Table S7, S8).

3.3.3. Numerical Implementation

The resulting system of equations describing the coupling between multicomponent transport of aqueous/solid species and chemical reactions was numerically solved with a finite element method (FEM) utilizing the finite element solver COMSOL Multiphysics (e.g., Rolle et al. 2018). Based on the chemical reaction network described in Table 2, we considered a total of 27 chemical species (Table S5, Supplementary Material) that are sufficient to illustrate the complete biogeochemistry of our system. In

Table 2
Chemical reaction pathways and stoichiometries implemented in the diagenetic model.

Primary redox reactions	
$OM^{\alpha,\beta} + a\ O_2 \rightarrow NH_4^+ + c\ H_3PO_4 + a\ H_2O$	R1
$OM^{\alpha,\beta} + \frac{4a}{5}\ NO_3^- + \frac{4a}{5}\ H^+ \rightarrow a\ CO_2 + b\ NH_4^+ + c\ H_3PO_4 + \frac{2a}{5}\ N_2 + \frac{7a}{5}\ H_2O$	R2
$OM^{\alpha,\beta} + 2\ a\ MnO_2^{\alpha} + 4\ a\ H^+ \rightarrow a\ CO_2 + b\ NH_4^+ + c\ H_3PO_4 + 2\ a\ Mn^{2+} + 3\ a\ H_2O$	R3
$OM^{\alpha,\beta} + 4\ a\ Fe(OH)_3^{\alpha} + 4\ a\chi^{\alpha}\ Fe_{ox}P + 12\ a\ H^+ \rightarrow a\ CO_2 + b\ NH_4^+\ (c + 4\ a\ \chi^{\alpha})\ H_3PO_4 + 4\ a\ Fe^{2+} + 13\ a\ H_2O$	R4
$OM^{\alpha,\beta} + \frac{a}{2}\ SO_4^{2-} + a\ H^+ \rightarrow a\ CO_2 + b\ NH_4^+ + c\ H_3PO_4 + \frac{a}{2}\ H_2S + a\ H_2O$	R5
$OM^{\alpha,\beta} \rightarrow \frac{a}{2}\ CO_2 + b\ NH_4^+ + c\ H_3PO_4 + \frac{a}{2}\ CH_4$	R6
$CO_2 + 4\ H_2 \rightarrow CH_4 + 2\ H_2O$	R7
Secondary redox and other reactions	
$2\ O_2 + NH_4^+ + 2\ HCO_3^- \rightarrow NO_3^- + 2\ CO_2 + 3\ H_2O$	R8
$O_2 + 2\ Mn^{2+} + 4\ HCO_3^- \rightarrow 2\ MnO_2^{\alpha} + 4\ CO_2 + 2\ H_2O$	R9
$O_2 + 4\ Fe^{2+} + 8\ HCO_3^- + 2\ H_2O + 4\ \chi^{\alpha}H_2PO_4^- \rightarrow 4\ Fe(OH)_3^{\alpha} + 4\ \chi^{\alpha}Fe_{ox}P + 8\ CO_2$	R10
$2\ O_2 + FeS \rightarrow SO_4^{2-} + Fe^{2+}$	R11
$7\ O_2 + 2\ Fe_S2 + 2\ H_2O \rightarrow 4\ SO_4^{2-} + 2\ Fe^{2+} + H^+$	R12
$2\ O_2 + H_2S + 2\ HCO_3^- \rightarrow SO_4^{2-} + 2\ CO_2 + 2\ H_2O$	R13
$2\ O_2 + CH_4 \rightarrow CO_2 + 2\ H_2O$	R14
$MnO_2^{\alpha,\beta} + 2\ Fe^{2+} + 2\ \chi^{\alpha}\ H_2PO_4^- + 2\ H_2O + 2\ HCO_3^- \rightarrow 2\ Fe(OH)_3^{\alpha} + 2\ \chi^{\alpha}\ Fe_{ox}P + Mn^{2+} + 2\ CO_2$	R15
$MnO_2^{\alpha,\beta} + H_2S + 2CO_2 \rightarrow Mn^{2+} + S_0 + 2\ HCO_3^-$	R16
$2\ Fe(OH)3^{\alpha} + 2\ \chi^{\alpha}Fe_{ox}P + H_2S + 4\ CO_2 \rightarrow 2\ Fe^{2+} + 2\ \chi^{\alpha}H_2PO_4^- + S_0 + 4\ HCO_3^- + 2\ H_2O$	R17
$2\ Fe(OH)3^{\beta} + 2\ \chi^{\beta}\ Fe_{ox}P + H_2S + 4\ CO_2 \rightarrow 2\ Fe^{2+} + 2\ \chi^{\beta}\ H_2PO_4^- + S_0 + 4\ HCO_3^- + 2\ H_2O$	R18
$Fe^{2+} + 2\ H_2S \rightarrow FeS + 2H^+$	R19
$FeS + H_2S \rightarrow FeS_2 + H_2$	R20
$4\ S_0 + 4\ H_2O \rightarrow 3\ H_2S + SO_4^{2-} + 2H^+$	R21
$FeS + S_0 \rightarrow FeS_2$	R22
$SO_4^{2-} + CH_4 + CO_2 \rightarrow 2\ HCO_3^- + H_2S$	R23
$CH_4 + 8\ Fe(OH)_3^{\alpha,\beta} + 8\ \chi^{\alpha,\beta}\ Fe_{ox}P + 15H^+ \rightarrow HCO_3^- + 8\ Fe^{2+} + 8\ \chi^{\alpha,\beta}\ H_2PO_4^- + 21\ H_2O$	R24
$Fe(OH)_3^{\alpha} + (\chi^{\alpha} - \chi^{\beta})Fe_{ox}P \rightarrow Fe(OH)_3^{\beta} + (\chi^{\alpha} - \chi^{\beta})H_2PO_4^-$	R25
$Fe(OH)3^{\beta} + (\chi^{\beta} - \chi^{\gamma})Fe_{ox}P \rightarrow Fe(OH)_3^{\gamma} + (\chi^{\beta} - \chi^{\gamma})H_2PO_4^-$	R26
$MnO_2^{\alpha} \rightarrow MnO_2^{\beta}$	R27
$MnO_2^{\beta} \rightarrow MnO_2^{\gamma}$	R28
$3\ Fe^{2+} + 2\ HPO_4^{2-} \rightarrow Fe_3(PO_4)_2 + 2\ H^+$	R29
$Fe^{2+} + CO_3^{2-} \rightarrow FeCO_3$	R30
$FeCO_3 + H_2S \rightarrow FeS + HCO_3^- + H^+$	R31
$Fe_3(PO_4)_2 + 3\ H_2S \rightarrow 3\ FeS + 2\ HPO_4^{2-} + 4\ H^+$	R32

all pockmarks, the simulation was performed for a period of 50 years. The pockmarks were modeled as 1-D reactive transport systems and any possible multidimensional effect was ignored for the sake of brevity. For the dissolved species, a fixed concentration boundary with the bottom water composition was applied at the sediment–water interface, whereas a flux boundary was employed for the solid components. In contrast, a zero gradient and a free flux boundary conditions were applied for the dissolved and particulate chemical species, respectively, at the bottom of the domain. In this step, the model depth was set long enough to avoid any potential interference of the lower boundary condition with the model results in the upper sediments. The simulations were performed as a forward modeling fashion without attempting any inverse modeling scheme. Pockmark B and D were simulated by considering a sediment groundwater discharge rate in the upward direction, whereas pockmark E was considered to be fully diffusion controlled. Such an assumption is justified because pockmark E shows rather constant Cl^- concentration profiles, resembling a negligible impact of groundwater discharge. A summary of the input parameters used in the simulation of different pockmarks are provided in the Supplementary Material (Table S4, S6, S8).

3.4. Research data

Geochemical and grain-size data of the sediment samples, and geochemical data of all the water samples are available in the PANGAEA repository (Virtasalo, 2022; Virtasalo et al., 2022). DNA sequences and related metadata are available at European Nucleotide Archive under study PRJEB44075, where archaeal sequence IDs are ERS6176640-ERS6176659 and bacterial sequence IDs ERS6177874-ERS6177845.

4. RESULTS

4.1. Pockmark sediment composition

The box core sediment samples collected from pockmarks B and D are composed of structureless, poorly sorted fine sand with very low carbon content (range 0.17–0.69 mmol g^{-1} TOC; Fig. 2). The sediment surface in both cores is covered by a thin layer of brownish organic-rich fluffy material (Supplementary Material, Fig. S1). In contrast, the gravity core from pockmark E is composed of very poorly sorted dark-grey clay that is rich in carbon (range 2.0–5.5 mmol g^{-1} TOC; Fig. 2). The clay

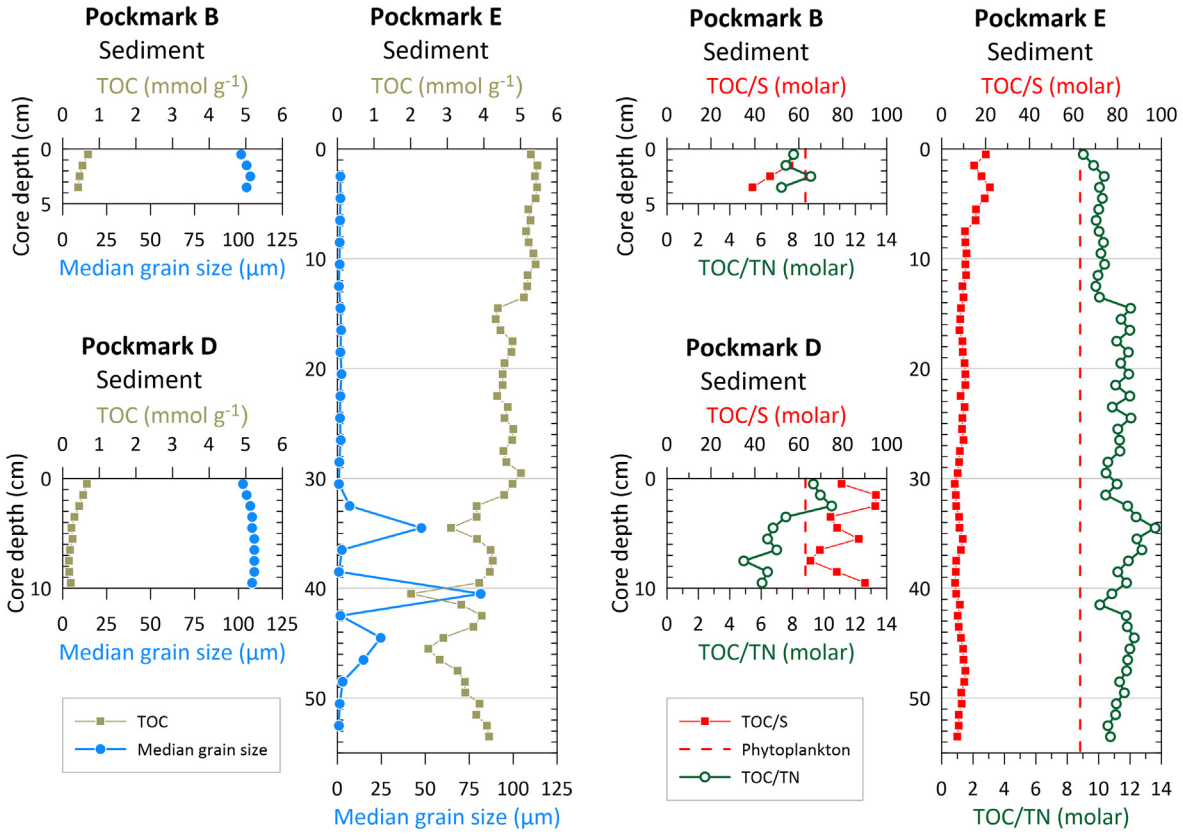

Fig. 2. Vertical distributions of TOC, median grain size, the TOC/S, and the TOC/TN ratio in sediment cores from pockmarks B, D and E. Red vertical dashed line indicates the mean TOC/S ratio of 63 of the Baltic Sea phytoplankton (Kumblad and Bradshaw, 2008). (For interpretation of the references to colour in this figure legend, the reader is referred to the web version of this article.)

is structureless with abundant plant fragments and a few thin interbeds of silt (Supplementary Material, Fig. S1). The sediment surface was dark grey at the time of coring, indicative of reducing conditions at the sediment–water interface.

The ^{137}Cs activity peak of 69.2 Bq kg^{-1} at the depth of 47–48 cm in the core from pockmark E is assigned the year 1986 (Supplementary Material, Fig. S2). Linear sedimentation rate in that core above this age-depth control point is calculated at 1.44 cm yr^{-1}. The interpreted depth of the year 1986 is supported by sediment Hg content, which shows a strong downward increase in the lower part of the core (Supplementary Material, Fig. S2). According to previous studies, Hg contents in the western Gulf of Finland are highest in sediment layers deposited in the early 1970 s and decline upwards (Vallius, 2014). Therefore, the pockmark E core must be younger than 1970 because the downward Hg increase likely continues below the core base. The ^{137}Cs contents in the cores from pockmarks B and D are at the background levels (<10 Bq kg^{-1}) except for the topmost 2–3 cm layers. The ^{137}Cs activity peak of 1986 seems not to be recorded in these cores.

The molar TOC/TN ratios are low in the cores from pockmarks B and D and range between 4.9 and 10.5, whereas the TOC/TN ratios are higher in the pockmark E core (range 9.0–13.6; Fig. 2). The TOC/S ratios are high in the pockmark B and D cores and range between 39 and 95, which is close to and above the mean ratio of 63 of the Baltic Sea phytoplankton (Kumblad and Bradshaw, 2008). The TOC/S ratios are lower in the pockmark E core (range 5.9–22) and show a downward decreasing trend.

4.2. Pockmark porewater, seawater and groundwater composition

Porewater Cl^- concentrations in the core from pockmark E are close to 100 mmol/L (Fig. 3), which is a typical value for the Baltic Sea water (Table 3). In contrast, porewater Cl^- concentrations are very low in pockmark D (range 0.21–7.62 mmol/L; measured salinity 0), indicating a strong fresh groundwater influence up to the sediment surface (groundwater Cl^- concentration 0.07–1.34 mmol/L). Pockmark B has intermediate porewater Cl^- concentrations that approach seawater values at the sediment surface (range 45.1–84.6 mmol/L; salinity range 2–6). Porewater SO_4^{2-} concentrations are low in pockmark D (range 0.08–0.41 mmol/L) and in the lower part of the core from pockmark E (Fig. 3). Porewater SO_4^{2-} concentrations increase strongly toward the core top in pockmark E, and in pockmark B, exceeding 3.5 mmol/L. Overall, SO_4^{2-} concentration profiles are similar to Cl^- concentration profiles in

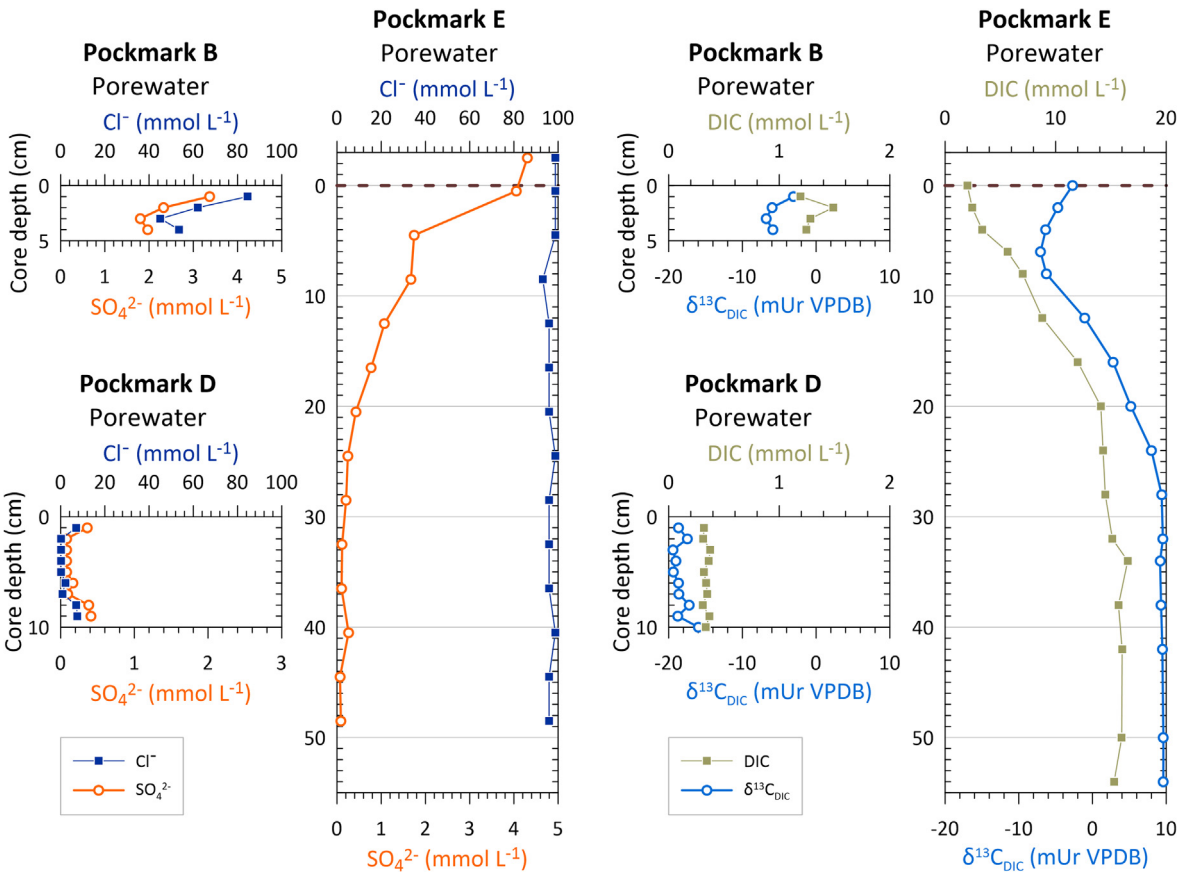

Fig. 3. Vertical distributions of Cl^-, SO_4^{2-}, DIC and $\delta^{13}C_{DIC}$ in sediment core porewater from pockmarks B, D and E. Dashed horizontal line indicates the sediment–water interface in the pockmark E core.

Table 3
Concentrations in the water column at the pockmark locations, the offshore station and in the groundwater.

Sampling sites	Sampling depth (m)	Cl^- (mmol/L)	S (mmol/L)	CH_4* (μmol/L)	NH_4^+ (μmol/L)
Pockmark B, active	2	83.2	3.80	0.047 +/− 0.006	0.7
	6			0.021 +/− 0.001	0.6
	10	101.5	4.61	0.021 +/− 0.0002	0.6
Pockmark D, active	2	97.3	4.24	0.035 +/− 0.003	0.0
	6			0.020 +/− 0.002	0.6
	10	100.1	4.58	0.006 +/− 0.0009	0.2
Pockmark E, inactive	2	88.9	3.98	0.027 +/− 0.002	0.4
	6			0.020 +/− 0.002	0.4
	10	100.1	4.60	0.021 +/− 0.0006	0.0
Offshore station J	2			0.035 +/− 0.004	0.5
Groundwater, observation well HP101		0.07	0.10	0.044 +/− 0.0008	0.7
Groundwater, obsolete water intake well		1.34	0.18	0.006 +/− 0.002	0.4

* Given as a mean +/− estimated standard deviation (see Bange et al., 2010) based on the CH_4 measurements of the triplicate water column and groundwater samples (see Section 3.1 Sample collection).

pockmarks B and D, whereas this is not the case for pockmark E.

Porewater DIC concentrations are low in pockmark D (range 0.31–0.38 mmol/L), whereas they are somewhat higher in pockmark B (range 1.2–1.5 mmol/L) and significantly higher in pockmark E (range 2.0–16.5 mmol/L; Fig. 3). Porewater DIC concentrations decrease strongly toward the core top in pockmark E. Porewater $\delta^{13}C_{DIC}$ values are strongly negative in pockmark D (from −19.4 to −16.0 mUr), and slightly negative in pockmark B (from −6.8 to −3.0 mUr; Fig. 3). Porewater $\delta^{13}C_{DIC}$ values are ca. + 9.5 mUr below the 25 cm depth in pockmark E and

decrease upward towards a pronounced minimum of −7.1 mUr at 6 cm depth, before increasing to −2.7 mUr at the sediment surface.

Porewater CH_4 concentrations are low in pockmark D (range 0.038–0.066 μmol/L), whereas they are higher in pockmark B (range 0.127–0.372 μmol/L) and orders of magnitude higher in pockmark E (949–1841 μmol/L below 5 cm depth; Fig. 4). We note that the values below 5 cm depth may be subject to outgassing of CH_4 from the sediment core on deck prior to porewater sampling (e.g., Egger et al., 2016a,b; Egger et al., 2017) and thus underestimate the true value. Porewater CH_4 concentrations decrease strongly toward the core top in pockmark E and reach 24.2 μmol/L above the sediment–water interface (Fig. 4). However, this value is still significantly elevated with respect to porewaters in pockmarks B and D. Similarly, porewater NH_4^+ concentrations are low in pockmark D (range 3.2–12.4 μmol/L) and higher in pockmark B (range 24.0–42.5 μmol/L; Fig. 4). Porewater NH_4^+ concentrations are much higher in pockmark E and show a strong upward-decreasing trend (range 166–1974 μmol/L).

CH_4 concentrations in the seawater column above the pockmarks, at the offshore station J and in the groundwater wells were in the range from 0.006 μmol/L to 0.047 μmol/L (Fig. 4; Table 3). Surface seawater samples from the depth of 2 m at the pockmark locations and at the offshore station J showed CH_4 concentrations between 0.03 and 0.05 μmol/L. Lower CH_4 concentrations of ca. 0.02 μmol/L were measured in the bottom (10 m) and intermediate-depth (6 m) samples from the pockmark locations, with a very low CH_4 concentration of 0.006 μmol/L in the bottom water at pockmark D. The groundwater observation well HP101 showed a CH_4 concentration of 0.04 μmol/L that is within the range of the sea surface water samples. The water intake well had a very low CH_4 concentration of 0.006 μmol/L.

4.3. Groundwater discharge rate estimates

The pore water Cl^- concentration profiles in pockmarks B and D exhibit typical concave shapes (Fig. 5) with a clear indication of steep concentration gradients from the top of the sediment layer located at the interface between the seawater and freshwater. In contrast, pockmark E shows minimal concentration gradient as suggested by the uniform profile along the depth. This transition in Cl^- concentra-

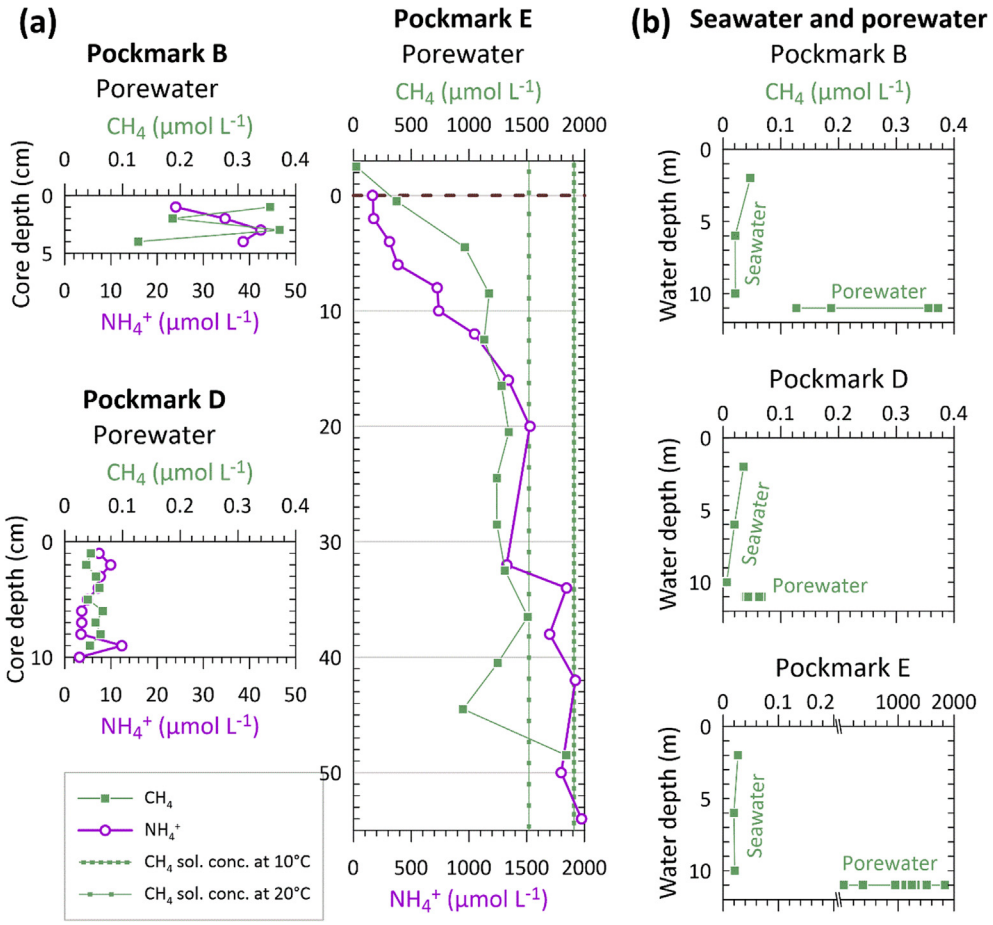

Fig. 4. Vertical distributions of CH_4, and NH_4^+ in sediment core porewater from pockmarks B, D and E (a) and CH_4 concentrations in the seawater column and porewater for pockmarks B, D and E(b). Dashed horizontal line indicates the sediment–water interface in the pockmark E core. Vertical lines indicate solubility concentration for CH_4 at the in-situ temperature of 10 °C and at 20 °C, calculated following Mogollón et al., (2013). Note the x-axis break in the pockmark E water column panel.

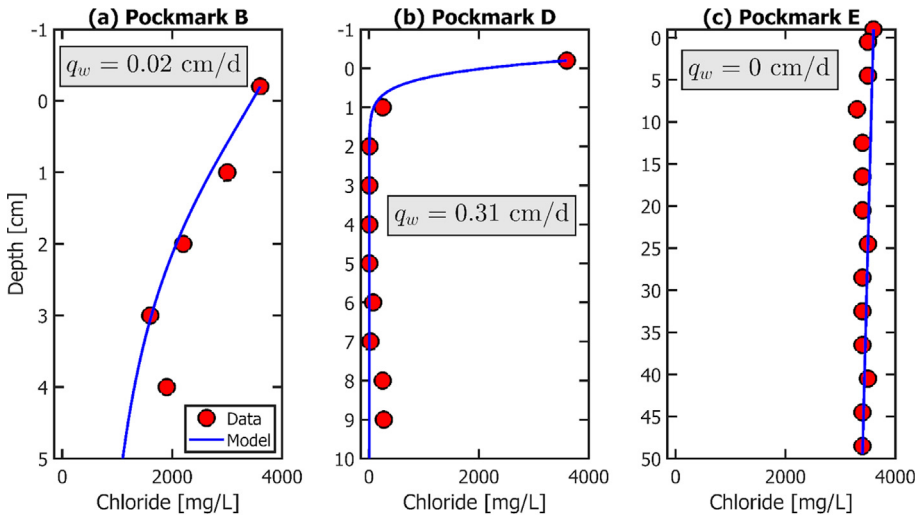

Fig. 5. Measured (markers) and simulated (lines) porewater chloride profiles along the depth in pockmarks B (a), D (b) and E (c).

tions along the sediment depth and the specific shape of the concentration profiles are ultimately controlled by the dynamic balance between the advective and diffusive/dispersive transport. Since chloride is chemically inert for most of the geochemical reactions occurring in these pockmarks, the observed Cl^- profiles were used to estimate the groundwater discharge rates across the seafloor. This was performed by fitting the chloride spatial profiles in different pockmarks against the analytical solution of the advection–dispersion equation as outlined in Section S2.

The results of the optimization performed with the least-squares curve fitting are summarized in Fig. 5 and Table S4 (Supplementary Material). The modelled porewater profiles indicate a clear trend of upward flow of freshwater in both pockmark B and D locations, while in pockmark E, no similar trend in the whole profile of 50 cm could be seen. It is also apparent that a relatively higher porewater specific discharge was obtained in pockmark D ($qw = 0.31$ cm d^{-1}) compared to that of pockmark B ($qw = 0.02$ cm d^{-1}, Table S4, Supplementary Material). Such behavior is consistent with the observed trends in their concentration profiles because freshwater front clearly migrates at a higher rate in pockmark D leading to the steepest concentration profile. In contrast, pockmark E shows a flat profile indicating the signature of inactive pockmarks, where transport processes are mainly driven by the diffusion mechanism from the sediment–water interface. Furthermore, pockmark B represents an intermediate system, where the behavior is collectively dominated by both the advective and diffusive fluxes. The groundwater discharge rates obtained from these fitting procedures were directly used in the reactive transport simulations presented in the next sections.

4.4. Total number of all microbes and functional groups

The total number of bacteria (using the 16S rRNA gene copy number as a proxy) varied between the sample types. Pockmark sediments contained the most microbes of any sample type. Bacterial 16S rRNA gene copy numbers ranged from 9.9×10^9-9.8×10^{10} (Table 4), of which pockmark E had the highest copy numbers. Total copy numbers of archaea ranged from 7.7×10^7 to 1.3×10^9, and as with bacteria, pockmark E contained the highest copy numbers. Compared between the different sampling depths, archaeal copy numbers were higher in the deeper sample in pockmark E, on a similar level in both depths in pockmark D, and higher in the shallower sample in pockmark B. Total copy numbers of bacteria in seawater samples above pockmarks was around 10^6 and archaea 10^4. In the offshore control site, archaeal copy numbers were 1.3×10^3, i.e., one order of magnitude lower than those above pockmarks. Groundwater samples contained the lowest number of microbes. Observation well 101 had 4.2×10^5 bacterial gene copies, while the obsolete water intake well had one order of magnitude less, 4.8×10^4 copies. Similarly, archaeal copy numbers were low, ranging from 614 in the observation well and 157 in the water intake well.

Potential metabolic functionality of microbes in sediments, groundwater and seawater were determined with quantitative PCR. Denitrifying consortium was measured using *nar*G gene as a proxy. The highest number of *nar*G genes was observed in the shallower sample of pockmark B (5.46×10^8) (Fig. 6, Supplementary Material, Table S3). The deeper sample from the same pockmark had 9.77×10^6 copies of *nar*G. A similar depth-related decreasing trend was observed in pockmark D, which had the overall lowest number of *nar*G copies in sediment samples. Second highest numbers were observed in pockmark E sediments, 3.24×10^7 in shallower and 8.94×10^7 in the deeper section. A decreasing trend in relation to sampling depth was also observed in *amo*A gene copies, proxy for ammonia oxidation, in pockmarks B and D. The copy numbers ranged from 10^8 to 10^6. In contrast, in pockmark E sediment *amo*A copy number was higher in deeper sediment, reaching 1.20×10^8, while the shallower sample had around one tenth of the copy number of *amo*A gene, 3.67×10^7 copies. *Nar*G and *amo*A gene copy numbers in all seawater samples were around 10^3, except *amo*A copies

Table 4
Number of 16S rRNA gene copies, sequencing statistics and ecological diversity, richness, evenness, dominance and abundance-based coverage estimates.

Sampling site	Total number of 16S rRNA gene copies		Total number of sequences		Observed OTUs		Coverage		Diversity						Richness			
									Shannon H'		Nonparametric Shannon		Inverse Simpson		Chao1		ACE	
	Bac	Arc	Bac	Arc	Bac	Arc	Bac	Arc	Bac	Arc	Bac	Arc	Bac	Arc	Bac	Arc	Bac	Arc
Seawater B, 1 m above pockmark	1.70E+06	1.82E+04	104,705	60,959	423	6	0.998	0.999	4.24	0.03	4.25	0.04	25.39	1.01	516.6	8.2	512.1	11.0
Seawater D, 1 m above pockmark	1.47E+06	2.54E+04	90,371	103,678	408	5	0.998	0.999	4.22	0.03	4.23	0.03	29.11	1.01	506.9	6.9	515.8	12.9
Seawater E, 1 m above pockmark	2.98E+06	3.20E+04	104,201	67,584	410	7	0.998	0.999	4.14	0.05	4.15	0.05	24.91	1.01	507.2	1.0	490.1	10.9
Seawater, offshore station J	2.51E+06	1.32E+03	108,308	2631	390	7	0.998	1.000	4.18	0.33	4.19	0.33	25.74	1.14	480.9	7.0	476.2	8.9
Pockmark B, active sediment, 1.5–2.5 cm depth	7.29E+10	1.37E+08	62,726	21,823	771	26	0.996	0.997	4.98	2.08	5.00	2.09	75.48	6.02	939.3	36.2	926.9	48.8
Pockmark B, active sediment, 3.5–4.5 cm depth	1.72E+10	7.73E+07	73,730	23,791	704	28	0.996	0.997	4.88	2.00	4.90	2.02	69.84	4.99	895.6	36.5	871.2	46.2
Pockmark D, active sediment, 1.5–2.5 cm depth	1.37E+10	4.80E+08	85,009	64,909	542	14	0.997	0.999	4.56	1.65	4.57	1.66	48.49	4.43	701.5	16.6	699.5	20.5
Pockmark D, active sediment , 3.5–4.5 cm depth	9.88E+09	4.43E+08	85,902	63,482	448	14	0.997	0.999	4.25	1.64	4.26	1.65	34.55	4.52	599.2	16.4	610.6	20.4
Pockmark E, inactive sediment, 1.5–2.5 cm depth	6.32E+10	5.35E+08	68,256	40,512	798	34	0.996	0.997	5.12	2.39	5.14	2.40	83.62	8.06	976.0	41.4	946.3	45.5
Pockmark E, inactive sediment, 3.5–4.5 cm depth	9.84E+10	1.34E+09	82,152	39,728	779	35	0.996	0.997	4.97	2.40	4.99	45.93	71.72	8.32	965.5	42.2	943.9	45.9
Groundwater, observation well HP101	4.21E+05	6.14E+02	88,174	8018	311	20	0.998	0.999	2.69	1.84	2.70	1.84	4.76	4.03	415.3	20.3	445.3	21.8
Groundwater, obsolete water station	4.84E+04	1.57E+02	98,431	n/a	323	n/a	0.998	n/a	3.01	n/a	3.02	n/a	8.82	n/a	392.0	n/a	389.0	n/a

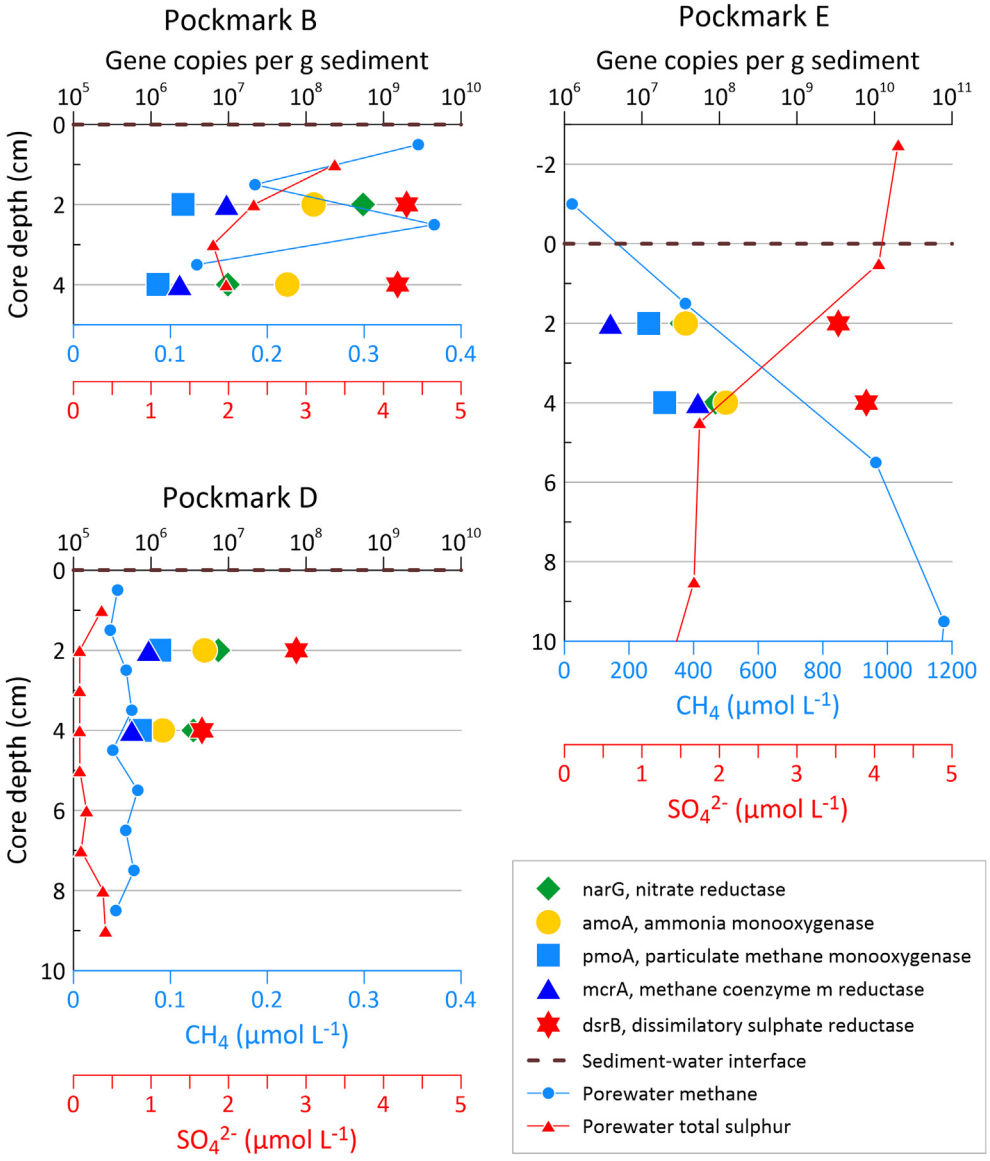

Fig. 6. Functional gene copy numbers of microbial populations in pockmark sediments, and concentrations of CH_4 and SO_4^{2-} in sediment porewaters. TS is interpreted to be mostly SO_4^{2-}.

were slightly lower in control seawater, 6.24×10^2 (Supplementary Material, Table S3). Groundwater samples had even lower copy numbers of *nar*G, 613 in HP101 and 55 copies in the water intake well near shoreline. Also, *amo*A copies in both groundwater samples were <100.

Methane cycling microbial consortia were identified with *pmo*A and *mcr*A. *Pmo*A is characteristic for the aerobic methane oxidation process, while the *mcr*A gene is functioning in both methanogens and anaerobic methane oxidizers. Pockmark E sediments had the highest numbers of *pmo*A genes (1.23×10^7 and 1.97×10^7 for the shallow and deep samples, respectively). Lowest numbers were detected from the deeper samples from pockmark B and D, 1.24×10^6 and 7.29×10^5, respectively. The highest number of *mcr*A copies were detected both in the deeper sample of pockmark E (5.25×10^7 gene copies) and from shallower sample from pockmark B (9.4×10^6 gene copies), although pockmark E had >1000 × higher methane concentrations. Pockmark D had lowest methane concentrations and lowest number of *mcr*A copies (on average 7.48×10^5). In seawater samples, *pmo*A copy number was 130 or less, and *pmo*A copies in groundwater samples were below detection limit (16 copies). *Mcr*A marker gene copies were on average 5.53×10^2 in seawater, and near the detection limit (49 copies or less) in groundwater.

The number of sulfate reducers, measured with *dsr*B marker gene, was overall highest of all functional groups determined in this study, and the highest number of sulfate reducers was detected in the deeper sample of pockmark E (7.88×10^9). However, the shallower sample from pockmark E and both samples from pockmark B were also at the 10^9 level. Pockmark D had clearly lower numbers of

*dsr*B copies, 7.48×10^7 (1.5–2.5 cm) and 4.53×10^6 (3.5–4.5 cm). Seawater from offshore station J had the highest amount of *dsr*B copies of all seawater samples, 4.26×10^4, and seawater samples above pockmarks ranged from 9.48×10^3 in pockmark E to 3.20×10^3 in pockmark D. Groundwater samples contained < 101 *dsr*B copies.

4.5. Microbial community diversity and composition

The dataset after quality control was composed of 2 299 000 (70 %) bacterial and 986 085 (30 %) archaeal sequences. Seawater samples had the highest number of bacterial sequences, ranging from 90 371 (above pockmark D) to 108 308 (seawater control sample from offshore station J) (Table 4). Conversely, the highest number of archaeal sequences (sample average of 103 678) was detected from seawater above pockmark D, while control seawater had the overall lowest number of archaeal sequences (2631). In sediments, the number of bacterial sequences ranged from 62 736 (pockmark B) to 85 902 (pockmark D) and archaeal numbers were 21 823 (pockmark B) to 64 909 (pockmark D). The number of bacterial sequences in groundwater samples were higher than in pockmark sediments but lower than in seawater, while archaeal sequence number in groundwater sample from observation well HP101 was lower than in sediments and seawater samples above pockmarks. Archaeal sequences were not retrieved from the obsolete water intake well.

Sediments had higher numbers of observed bacterial OTUs compared to groundwater and seawater samples (Table 4). Between the different sediment depths, the number of sequences retrieved from deeper sediment in pockmarks B and E was higher than in shallow samples. In pockmark D, there was no significant difference between the two sampling depths. Observed archaeal OTUs were much less than bacterial OTUs, and most OTUs were observed from sediments.

Rarefaction analysis showed that the archaeal community was extensively sequenced in most of the samples as rarefaction curves reached a plateau (Supplementary Material, Fig. S3). However, pockmark E and B rarefaction curves remained exponential, so these were not exhaustive sequenced. Similarly, rarefaction curves of bacterial communities (Supplementary Material, Fig. S4) in pockmark E and B, as well as the upper section of sediment in pockmark D remained exponential.. Rarefaction curves for sequences of bacterial communities from other samples showed that most of the diversity of the bacterial community in these had been captured by sequencing. Sequencing coverage for both archaeal and bacterial communities was high, ranging from 0.996 in bacteria in pockmark B and E to 1.000 in offshore station J seawater archaea (Table 4).

The most diverse environment studied was the pockmark sediment, according to all diversity indices (Shannon's H' diversity index, nonparametric Shannon and inverse Simpson index) (Table 4). Both archaeal and bacterial diversity was highest in pockmark E sediments, second highest in pockmark B and third highest in pockmark D. Seawater bacterial communities were nearly as diverse as those in pockmark D, but archaeal diversity was significantly lower in seawater samples than in other samples. Groundwater communities exhibited the lowest bacterial diversity. Species richness according to Chao1 richness index was highest in pockmark E, then pockmark B and D sediments. Seawater samples had equivalent bacterial species richness, lower than in sediments but higher than in groundwater. Archaeal species richness was, on the contrary, higher in groundwater than in seawater, and also in pockmark D sediment. Abundance-based coverage estimates (ACE) followed similar trends as Chao1 richness estimates.

Archaeal community structure varied between the different locations and samples. In class level comparison, the most abundant archaeal class was *Nitrososphaeria* that was detected in all samples but was most dominant in seawater samples taken above pockmarks, and least abundant in pockmark E sediment (Fig. 7). The most common OTU belonging to *Nitrososphaeria* class in seawater, pockmark B and E sediments was affiliating with *Candidatus* Nitrosopumilus, while in pockmark D sediment, another OTU affiliated with *Nitrosopumilaceae* was the most common OTU in this class (Supplementary Material, Krona charts "Arch_sed", "Arch_SW", "Arch_GW"). In addition, *Candidatus* Nitrosotalea -affiliating OTU was also abundant in pockmark D sediment and in groundwater from the observation well. The most abundant OTU in groundwater, belonging to *Nitrososphaeria* class, affiliated with *Nitrosoarchaeum*. *Nanoarchaeia* was the second-most dominant class, especially abundant in pockmark sediments, and of all samples, most abundant in pockmark E. Abundant OTUs in this class affiliated with *Woesearcheales*. Bathyarchaea were the most abundant in the lower section of pockmark B sediment, but also detected from pockmark E and groundwater samples. Methanogenic archaeal classes, *Methanomicrobia* and *Methanosarcinia* were mainly detected in pockmark E. Methanomicrobial OTUs were related to *Methanogenium*, *Methanospirillum*, *Methanocorpusculum*, *Methanolinea*, *Methanoregula* and *Methanoculleus*. OTUs affiliating with *Methanosarcina*, *Methanolobus*, *Methanosaeta* and ANME-2a-2b represented the *Methanosarcinia* class. *Thermoplasmata* -affiliating OTUs were abundant in pockmark E and in the lower sample of pockmark B. The groundwater sample community was composed of OTUs belonging to unclassified Crenarchaota and many low abundance OTUs in addition to the abovementioned *Candidatus* Nitrosotalea and *Nitrosoarchaeum*.

Gammaproteobacterial OTUs were the most abundant group in all pockmark sediments (Fig. 8). A detailed taxonomic inspection showed that many of these were affiliated with *Comamonadaceae* and *Nitrosomonadaceae* (Supplementary Material, Krona chart "Bac_sed"). In comparison to other sediments, abundant bacteria in sediment D communities were affiliating with *Nitrospira*, the actinobacterial MB-A2-108 group and unclassified bacterial OTUs. In addition, *Gemmatimonadales* -affiliating OTUs were more common in pockmark D than in other pockmark sediments. Alphaproteobacteria represented higher relative abundance in pockmark D, with *Rhizobiales* a major group. In pockmarks B and E, alphaproteobacterial *Rhodobacteraceae* were abundant in addition to *Rhizobiales*. Similarly to

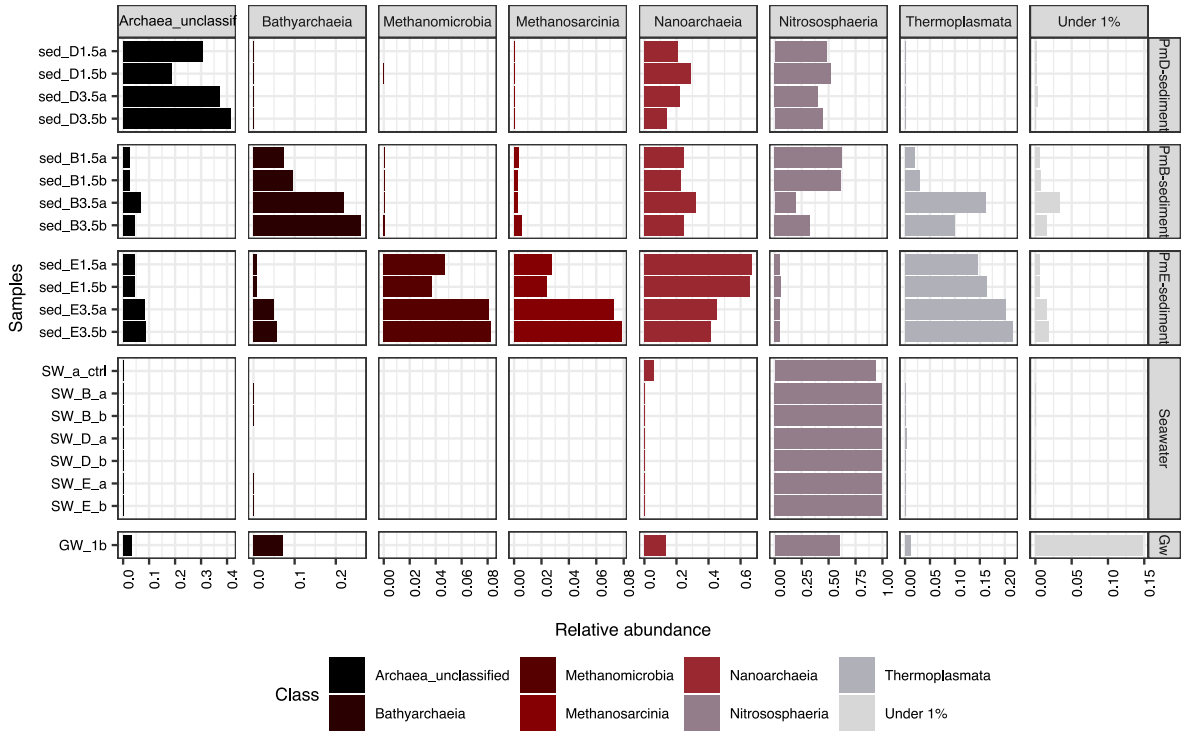

Fig. 7. Class level archaeal diversity in sediments (sed), seawater (SW) and groundwater (GW). Pockmarks (*Pm*) are labeled D, B and E, and 1.5 or 3.5 correspond to the depth in cm from which they were retrieved. Lowercase a and b mark the duplicate samples. Note that the relative abundance scale in × axis is different between panels, compare samples inside class, not between classes.

Alphaproteobacteria, pockmark D sediment hosted a relatively higher abundance of Burkholderiales compared to pockmarks B and E. *Polyangia* and *Thermoleophilia* had similar abundances in pockmark D and B, while typical sulfate reducer classes *Desulfobacteria* (*Desulfosarcina* and *Desulfosarcinaceae* OTUs) and *Desulfobulbia* (*Desulfocapsaceae*, *Desulfobulbaceae* and *Desulforhopalus* OTUs) were abundant in pockmarks B and E. Bacteroidia were equally abundant in seawater samples and in the upper layer of sediment E, however these were not represented by the same OTUs. Rare OTUs (representing <1% of the total community) were common in all sediment samples, but less abundant in seawater and groundwater samples. Seawater communities were composed mainly of Gammaproteobacteria (*Pseudohongiella*, *Methylophilaceae*), Bacteroidia (*Fluviicola*, *Sphingobacterales* and *Flavobacterales* -affiliating OTUs), Alphaproteobacteria (*Pseudorhodobacter*), Actinobacteria (*Sporichthyaceae* -affiliating OTU) and Acidimicrobia (*Ilumatobacteraceae* OTU) (Supplementary Material, Krona chart "Bac_SW"). Gammaproteobacteria (*Pseudomonas*, *Rhodoferax*, *Undibacterium* OTUs) were the main component of groundwater from HP101, while Alphaproteobacteria (*Brevundimonas* and *Caulobacter* -affiliating OTUs) and gammaproteobacterial *Hydrogenophaga* dominated the obsolete water intake well groundwater community (Supplementary Material, Krona chart "Bac_GW).

Diversity between the samples was visualized with PCoA plots. Using Bray-Curtis dissimilarity index based on abundance estimates and Jaccard index based on presence/absence of species, different sample types divide clearly into separate groups (Fig. 9). Looking into archaeal (Fig. 9a,c) and bacterial (Fig. 9b,d) communities in different samples, pockmarks E and B group together, but are separate from pockmark D, seawater sample, and groundwater samples. The main observations are reproduced in both the Bray-Curtis and Jaccard index approaches to the PCoA.

5. DISCUSSION

This study investigates biogeochemistry and microbial community structure in three pockmarks formed by SGD. Pockmarks B and D were formed in fine sand on the slope of a shore platform at the water depth of 11 m and ca. 200 m from shoreline. Pockmark E was also formed in fine sand but has later been passively covered by organic-rich mud. Previous ^{222}Rn measurements of near-bottom water showed that pockmarks B and D are sites of active groundwater discharge, whereas pockmark E is currently inactive (Virtasalo et al., 2019). Below we discuss the contrasting biogeochemical settings and microbial communities of the different sites, before considering the broader implications of our findings.

5.1. Biogeochemical setting

The sediment and porewater geochemical characteristics indicate a contrasting set of early diagenetic processes between the active pockmarks (B, D) and the inactive

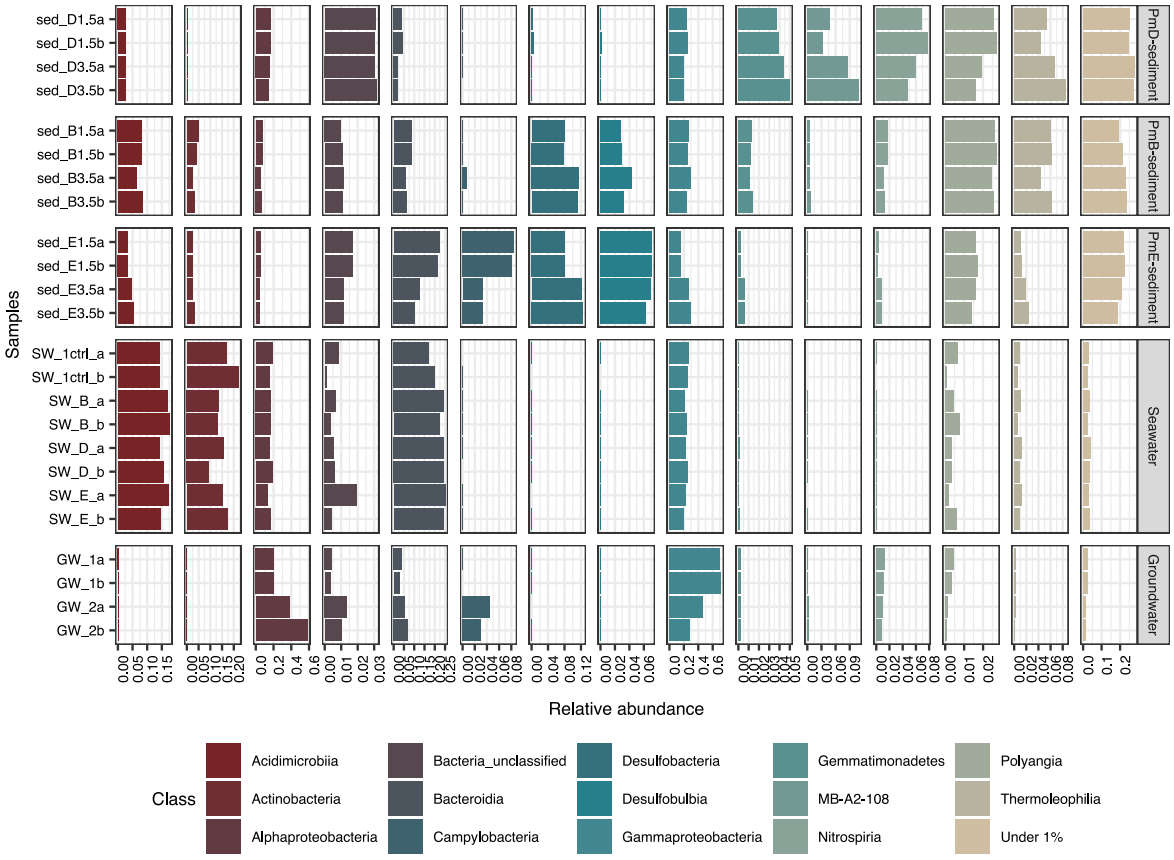

Fig. 8. Class level bacterial diversity in sediments (sed), seawater (SW) and groundwater (GW). Pockmarks (*Pm*) are labeled D, B and E, and 1.5 or 3.5 correspond to the depth in cm from which they were retrieved. Lowercase a and b mark the duplicate samples. Note that the relative abundance scale in × axis is different between panels, compare samples inside class, not between classes. In the legend, each panel of 3 classes corresponds to the above three facets.

pockmark (E). At pockmark E, insignificant groundwater contribution was calculated from the Cl^- profile (Fig. 5). The porewater diagenetic zonation at this site is strongly reminiscent of typical organic matter-rich muddy seafloor in this area, as described in several recent studies (Jilbert et al., 2018; Myllykangas et al., 2020a; Jokinen et al., 2020) and consistent with early diagenesis in a brackish setting with a limited amount of dissolved sulfate in the bottom waters (Froelich et al., 1979; Jørgensen and Kasten, 2006). The setting is characterized by compressed zones of oxic and suboxic remineralization close to the sediment–water interface, and a shallow sulfate-methane transition zone (SMTZ), reflecting the high demand for electron acceptors for anaerobic remineralization of organic matter. Accordingly, pockmark E sediments were enriched in TOC, at >4% throughout most of the profile (Fig. 2), and porewaters displayed high concentrations of NH_4^+ and DIC (up to >1500 μM and >15000 μM, respectively), the principal metabolites from organic matter remineralization. Sediment TOC/S ratio was also low at pockmark E (Fig. 2) indicating pyrite formation (Berner, 1970) as well as sulfurization of organic matter (Brüchert, 1998; Passier et al., 1999, Werne et al., 2008) during early diagenesis. In contrast, significant groundwater contribution was calculated from the Cl^- profiles of pockmarks B and D (Fig. 5). Lower TOC contents and negligible accumulation of metabolites (DIC, NH_4^+) in the porewaters suggest that early diagenetic processes exert a less important control on porewater chemistry at pockmarks B and D (Figs. 3, 4), supporting the interpretation of an advection-dominated system. There is thus no indication of the development of a SMTZ as observed at pockmark E, and much less indication of enrichment of sediments with sulfur (TOC/S weight ratios 40–60 and 60–90 at B and D, respectively; Fig. 2). In general, the contrast between low rates of diagenetic processes in active pockmarks and high rates in the surrounding sediment environments resembles the result of Whiticar (2002) for similar investigation in Eckernförde Bay.

The reactive transport simulations capture the essential features of the porewater (Fig. 10) and solid-phase profiles (Fig. 11) and confirm the overall contrast between the active and passive pockmarks. The model was able to simultaneously reproduce the spatial concentration profiles of most chemical species observed in each pockmark. We note that the poor fit of the CH_4 data from pockmark E below 10 cm depth (Fig. 10n) may reflect the impact of degassing from the sediment core during sampling, leading to underestimated concentrations in the deeper part of the core (e.g., Egger et al., 2016a,b; Egger et al., 2017). The effects of the diagenetic processes and biogeochemical

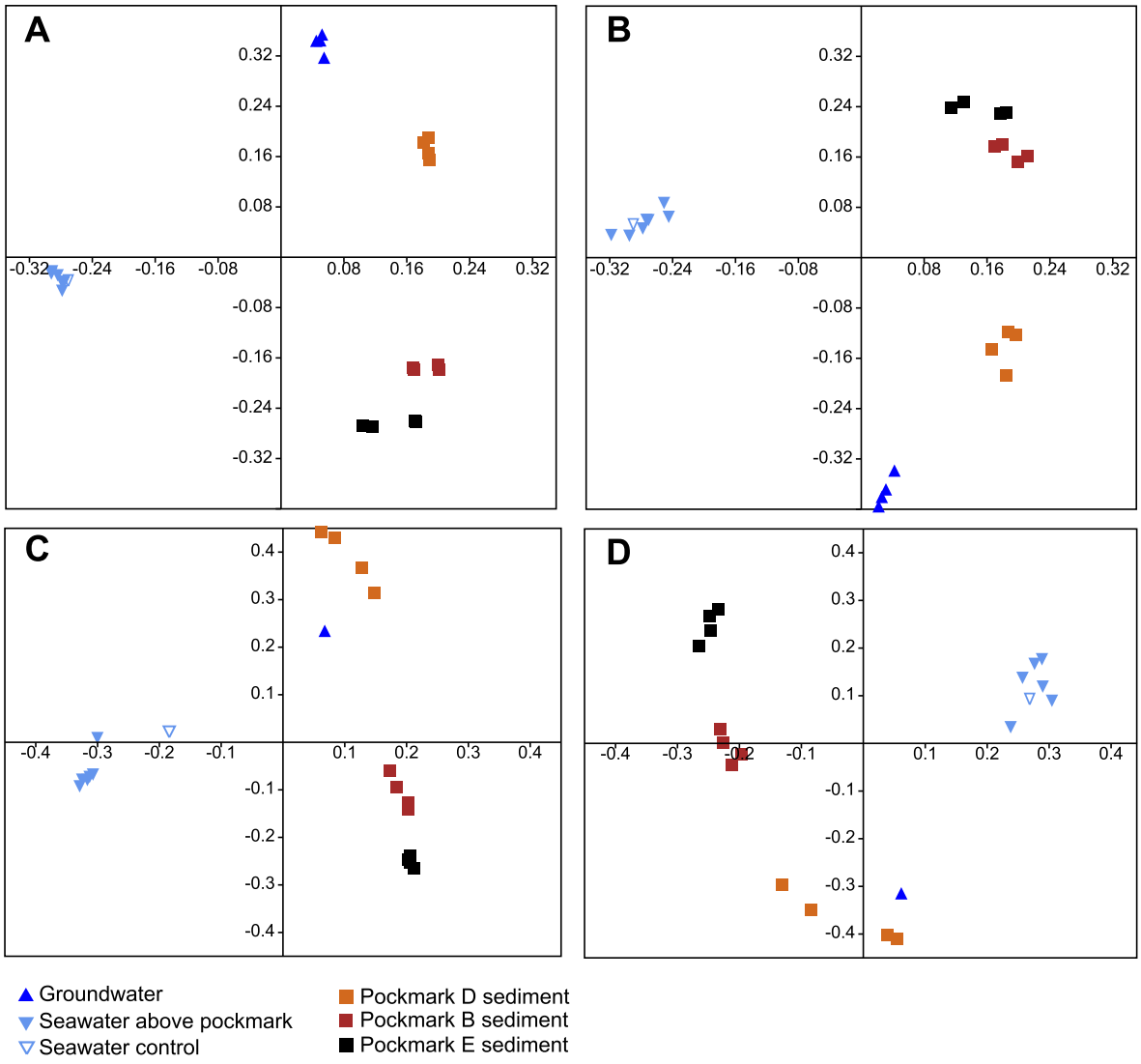

Fig. 9. Bray-Curtis -based PCoA of archaeal (A) and bacterial (B) OTUs. Jaccard -based PCoA of archaeal (C) and bacterial (D) OTUs.

reactions are clearly evident in the solute concentration profiles because SO_4^{2-} (which is a reactant in primary redox reactions) concentrations show a clear trend for consumption (second column panels, Fig. 10) with sediment depth, compared to the conservative chloride species. This effect is most pronounced in pockmark E (first column panels, Fig. 10). A similar trend is also observed in the modeled profiles of other electron acceptor species (results not shown). In contrast, NH_4^+, CH_4, and DIC profiles indicate a signature for gradual production of these species with depth due to OM degradation reactions, leading to an outgoing solute flux across the sediment–water interface (third to fifth column panels, Fig. 10).

The model output shows that the contrasting profiles of metabolites such as NH_4^+, CH_4 and DIC between the pockmarks can be explained by the variable influence of SGD. Discharge rates can affect the accumulation of organic matter and other sediment phases (being much higher at pockmark E), but also the availability of porewater oxidants such as O_2 and SO_4^{2-} for primary redox reactions due to upwards advective flow. Furthermore, the upward advective flow in pockmarks B and D drives the transport of the reaction products to the upper active oxidation zone (top ca. 2 cm), where these species are further consumed by the secondary reactions and the available oxidants in the shallow depths (Fig. 10c-e, h-j). In contrast, this vertical recirculation does not occur in pockmark E, leading to orders of magnitude higher concentration levels for these species in deeper layers (Fig. 10m-o). The model also confirms that a direct correlation exists between these species' concentrations and the magnitude of the upward water flux, with the lowest concentration magnitude observed in pockmark D, which represents the highest SGD rate. The situation is opposite in pockmark E, where groundwater discharge was nonexistent, and the behavior of pockmark B lies in between these two cases.

Fig. 11 shows a comparison between the observed and simulated TOC and TN profiles in the solid phase for differ-

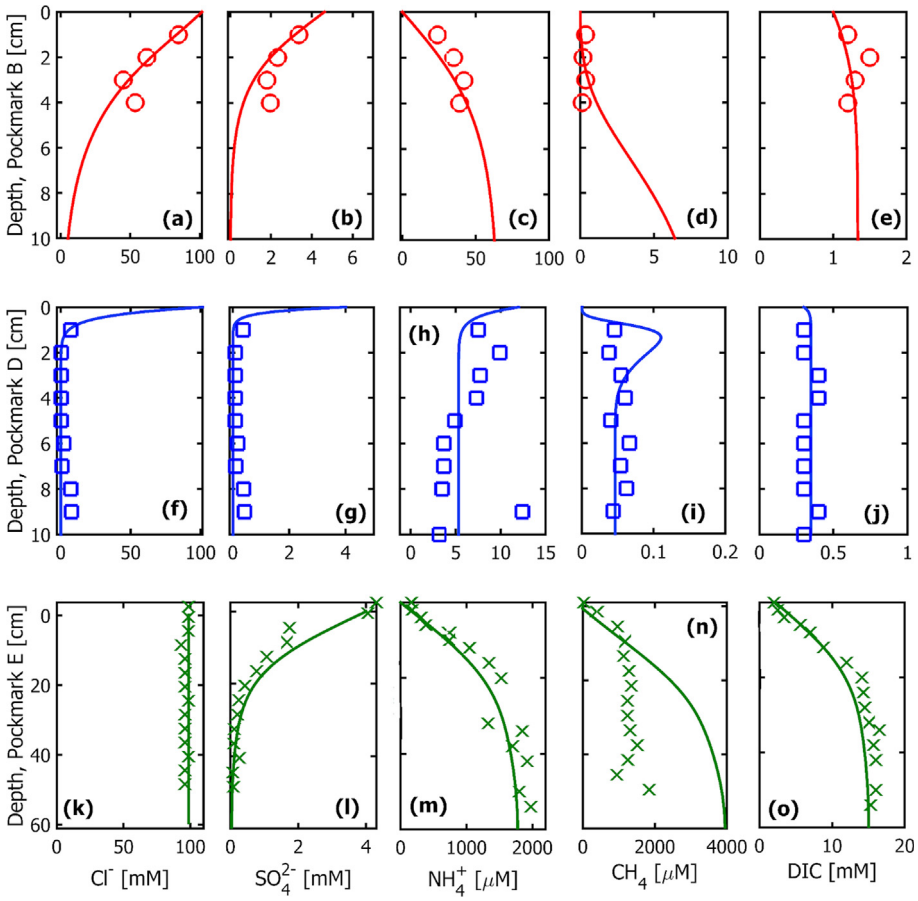

Fig. 10. Observed (symbols) and modeled (lines) porewater profiles for Cl^- (a,f,k), SO_4^{2-} (b,g,l), NH_4^+ (c,h,m), CH_4 (d,I,n), and DIC (e,j,o) from pockmarks B (top row panels, a-e), D (middle row panels, f-j) and E (bottom row panels, k-o). The measured porewater CH_4 concentrations are expected to be lower than the in-situ values due to degassing from the sediment core during sampling (e.g., Egger et al., 2016a,b; Egger et al., 2017).

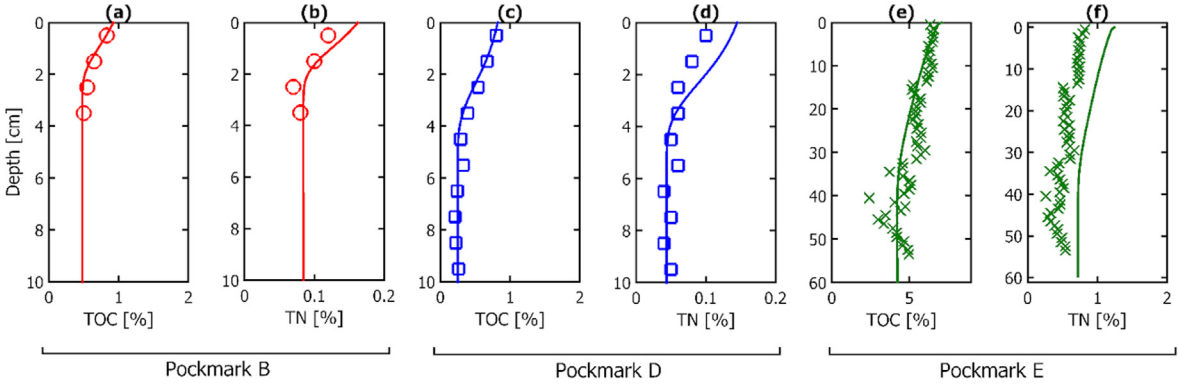

Fig. 11. Observed (symbols) and modeled (lines) solid-phase carbon (a,c,e) and nitrogen (b,d,f) profiles from pockmarks B (a-b), D (c-d) and E (e-f).

ent pockmarks. The model could reproduce the sediment concentration profiles for all the cases except for a minor disagreement for TN in pockmark E (Fig. 11f). This can be explained by the uncertainty related to the conceptualization of the initial definition of C:N:P ratio of the organic matter in the model. The effects of sedimentation rate are apparent in these profiles as an incoming front is clearly observed from the top boundary of the domain for both elements, implying constant sedimentation. Deposition of organic matter and other sediment components is expected at the inactive pockmark due to lower energy setting, but the addition of organic matter in the surface layer at the

active pockmarks is noteworthy. Mixing of organic-rich fluffy material by wave action to the sediment surface layer of pockmarks B and D may provide a mechanism for constant incorporation of low amounts of organic matter in the top 1–2 cm at these sites (Huettel et al., 1996). Indeed, images of the sediment surface in box cores at these pockmarks document the presence of fluffy organic material on the sediment surface (Supplementary Material, Fig. S1). It was necessary to consider sedimentation to occur at all pockmarks in order to model the observed profiles, with a temporally constant sedimentation rate sufficient to match the measured solid phase profiles. The model also confirms a much higher sedimentation rate in pockmark E (0.43 cm yr^{-1}) compared to that of pockmark B and D (3×10^{-7}, Supplementary Material, Table S4), as also validated with the ^{137}Cs activity measurements (Section 4.1). Such contrasting sedimentation rates are also evident in the solid phase concentration profiles, because both the TOC and TN fronts propagated up to a depth of ~40 to 50 cm in pockmark E (Fig. 11e-f), whereas these fronts moved only until ~2–3 cm depth in the two active pockmarks (Fig. 11a-d).

The model also allows a deeper inspection of the reactive transport mechanisms by facilitating the quantification of solute fluxes and biogeochemical process rates in the depth domain at each pockmark (Fig. 12). For brevity, we visualize the flux and reaction rate profiles only for SO_4^{2-} and CH_4, which are key reactants and products, respectively, with respect to the geochemical system studied. The model output confirms that diffusive fluxes dominate solute transport at the inactive pockmark E, while advective fluxes contribute to upwards transport of both SO_4^{2-} and CH_4 at the active pockmarks B and D (Fig. 12, left two column panels). The highest advective fluxes (green dash-dotted lines) of SO_4^{2-} are observed close to the sediment–water interface at pockmark D ($>1 \times 10^{-7}$ mol $m^{-2}s^{-1}$), where the strong upwards flow of groundwater (Fig. 5) is much stronger than the downwards diffusion (red dashed lines) of SO_4^{2-} from the bottom water. However, the situation is different for the reaction products (e.g., CH_4) as the produced solute quantities generally imply an upward diffusive flux from the active reaction zone to the upper boundary. Consequently, the advective and diffusive flux components act in an additive fashion leading to a higher total flux (blue solid lines) in most locations of the simulation domain (second column panels, Fig. 12).

With respect to biogeochemical process rates, strong contrasts are also observed between the pockmarks. The observation of a shallow SMTZ at pockmark E suggests important roles for both sulfate reduction and methanogenesis in organic matter remineralization at this site. The modeling results confirm that rates of both processes are orders of magnitude higher at pockmark E than pockmarks B and D (maximum rates up to 5×10^{-8} mol/m^{-3} s^{-1}). Furthermore, the zones of sulfate reduction and methanogenesis overlap in the depth domain (Fig. 12, right column panels), as commonly observed in diffusion-dominated coastal sites with high rates of organic matter deposition (e.g., Thang et al., 2013; Sawicka and Brüchert, 2017). In contrast, high groundwater discharge rates at the active pockmarks shift the reaction fronts upwards into rather compressed zones close to the sediment–water interface and enhance the sediment–water fluxes. This is most pronounced at pockmark D, where sulfate reduction and methanogenesis are limited to the uppermost 4 cm of the sediment column (Fig. 12).

In sedimentary settings where upwards diffusing methane meets downwards-diffusing sulfate at the SMTZ, sulfate-mediated anaerobic oxidation of methane (S-AOM) is expected to occur, thus dividing the consumption of sulfate between OM remineralization and methane oxidation (e.g., Jørgensen et al., 2019). The model output shows that S-AOM occurs at pockmark E in a similar depth range to organoclastic sulfate reduction (Fig. 12, right). Estimated rates of S-AOM in the model account for approximately 10% of total sulfate consumption at this depth. Furthermore, the effects of iron-mediated anaerobic oxidation of methane (Fe-AOM) are also visible in the active pockmarks (Fig. 12d, h). According to the model, Fe-AOM rates become increasingly important at greater depths in pockmark B and D, whereas the consumption of CH_4 due to Fe-AOM is almost negligible compared to the other mechanisms in pockmark E. Table 5 summarizes the simulated fluxes and reaction rates for selected species.

Further evidence for the presence of S-AOM at pockmark E is given by a combined analysis of porewater SO_4^{2-}, DIC and δ^{13}C-DIC data, following the modified Rayleigh-evaluation approach of Miller et al. (2017). The first part of the analysis employs the principle that the balance between dissimilatory sulfate reduction and S-AOM is reflected in the ratio of change in sulfate (ΔSO_4^{2-}) to change in dissolved inorganic carbon (ΔDIC), where *change* refers to the offset from the bottom water value at a given depth in the porewaters (Kastner et al., 2008; Hu et al., 2015; Wu et al., 2018). SMTZ environments dominated by S-AOM yield theoretical ratios close to 1, while those dominated by dissimilatory sulfate reduction yield theoretical ratios close to 2, due to the differing stoichiometries of sulfate consumption and DIC production between the two reactions. Miller et al. (2017) added the parameter DIC*δ^{13}C-DIC, a concentration-normalized expression of the stable carbon isotopic ratio of DIC, to a second part of the analysis, with the logic that deviations to negative δ^{13}C-DIC coincident with low $\Delta DIC/\Delta SO_4^{2-}$ provide supporting evidence for S-AOM due to the transfer of isotopically light C from CH_4 to DIC.

The results of the analysis show evidence for a contribution of S-AOM to total sulfate reduction in the depth interval corresponding to the SMTZ (0–10 cm) at pockmark E. This interval shows $\Delta DIC/\Delta SO_4^{2-}$ values of consistently < 2 (Fig. 13a). The same samples are characterized by negative DIC*δ^{13}C-DIC (Fig. 13b, seen also as a negative δ^{13}C-DIC excursion in Fig. 3). This evidence supports the interpretation of S-AOM in this interval. We note, however, that the absolute value of the negative δ^{13}C-DIC excursion is less extreme than often observed in fully marine SMTZ settings (e.g., Whiticar, 1999), due to dilution of the signal by concurrent methanogenesis (Jilbert et al., 2021). In contrast to pockmark E, the active pockmarks B and D show negative

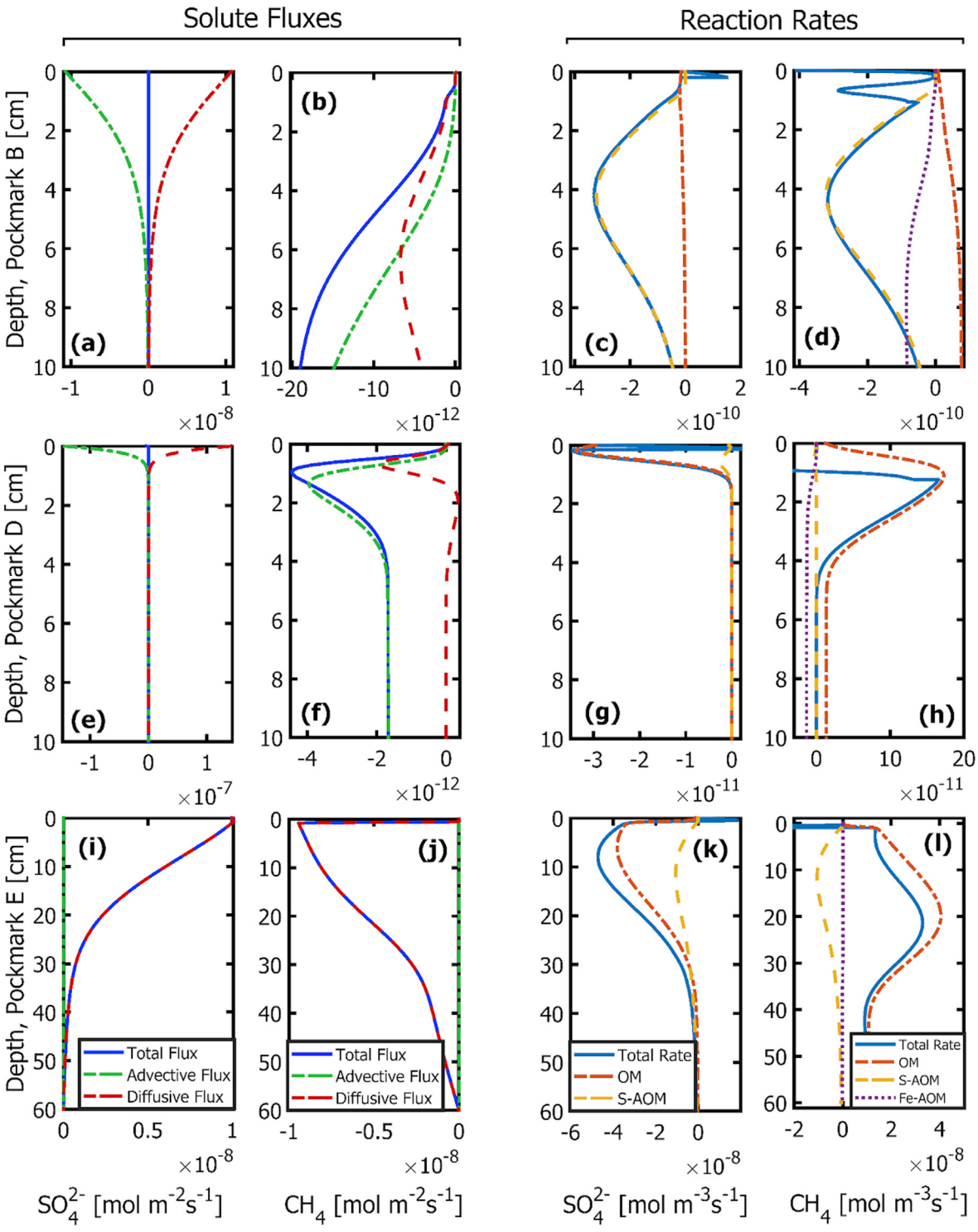

Fig. 12. Modeled flux components (left two column panels) and reaction rates (right two column panels) of SO_4^{2-} (first and third column panels) and CH_4 (second and fourth column panels) at sites B (a-d), D (e-h) and E (i-l): modeled rates of SO_4^{2-} consumption, CH_4 production and CH_4 consumption by different processes in the reaction network. OM = coupled to remineralization of organic matter; S-AOM = sulfate-mediated anaerobic oxidation of methane; Fe-AOM = Fe-oxide mediated anaerobic oxidation of methane.

values for ΔDIC, reflecting the lower values of DIC in porewaters compared to bottom waters and confirming the lack of evidence for significant rates of diagenetic processes.

Porewater CH_4 concentrations in all three pockmarks were significantly higher than the dissolved CH_4 concentrations measured in the seawater column above pockmarks

Table 5
Summary of fluxes and reaction rates for different pockmarks.

Quantity	Species	Integrated over depth[#] [mol m^{-1} s^{-1}] / [mol m^{-2} s^{-1}]*			Value at sediment–water interface [mol m^{-2} s^{-1}] / [mol m^{-3} s^{-1}]*		
		Pockmark			Pockmark		
		B	D	E	B	D	E
Flux	SO_4^{2-}	9.71×10^{-13}	2.10×10^{-13}	1.44×10^{-9}	2.37×10^{-11}	1.92×10^{-11}	1.01×10^{-8}
	CH_4	9.96×10^{-13}	2.03×10^{-13}	2.34×10^{-9}	1.14×10^{-13}	4.80×10^{-14}	8.00×10^{-13}
	NH_4^+	1.55×10^{-11}	1.92×10^{-11}	1.15×10^{-9}	-1.85×10^{-10}	-2.03×10^{-10}	-6.06×10^{-9}
	DIC	3.13×10^{-10}	1.25×10^{-9}	5.11×10^{-9}	-3.36×10^{-9}	-1.26×10^{-8}	-1.30×10^{-7}
	NO_3^-	1.12×10^{-12}	3.57×10^{-13}	7.99×10^{-12}	1.80×10^{-10}	9.41×10^{-11}	2.80×10^{-10}
Reaction rate	SO_4^{2-}	1.87×10^{-11}	1.75×10^{-13}	1.02×10^{-8}	-1.16×10^{-11}	-3.02×10^{-11}	-9.38×10^{-10}
	CH_4	1.91×10^{-11}	7.21×10^{-12}	1.96×10^{-8}	-4.09×10^{-10}	-1.96×10^{-10}	3.76×10^{-10}
	NH_4^+	3.30×10^{-11}	1.21×10^{-11}	7.37×10^{-9}	5.00×10^{-9}	-1.84×10^{-9}	2.92×10^{-7}
	DIC	2.56×10^{-10}	1.60×10^{-10}	5.35×10^{-8}	3.35×10^{-8}	3.34×10^{-8}	1.94×10^{-6}
	NO_3^-	1.81×10^{-10}	1.02×10^{-10}	2.15×10^{-9}	-2.36×10^{-8}	-1.68×10^{-8}	-1.14×10^{-7}

[#] The depth-integrated quantities were calculated using the absolute values of fluxes and reaction rates without explicitly considering their sign/direction: i.e., using $\int_0^L |J_i|dx$ for fluxes and $\int_0^L |R_i|dx$ for reaction rates.
* The first one refers to the unit of fluxes, whereas the second one indicates the unit of reaction rates.

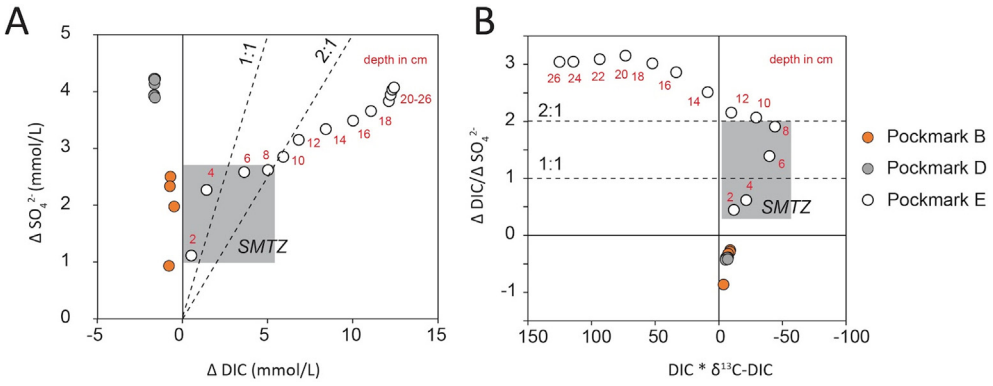

Fig. 13. A. Relationship between change in sulfate (ΔSO_4^{2-}) and change in dissolved inorganic carbon (ΔDIC), estimated for each porewater sample (for pockmark E, only the uppermost 26 cm are reported) relative to non-groundwater influenced near-bottom water data. Positive values of ΔDIC indicate an enrichment relative to near-bottom water, while positive values of ΔSO_4^{2-} indicate a depletion. B. Relationship between the ratio $\Delta DIC/\Delta SO_4^{2-}$ and the parameter DIC*δ^{13}C-DIC, a concentration-normalized expression of the stable isotopic ratio of DIC, for the same samples. In both A and B, depth (cm) of each sample at pockmark E is indicated in red, while 1:1 and 2:1 ratios of $\Delta DIC/\Delta SO_4^{2-}$ are indicated with dashed lines. Samples falling within the sulfate-methane transition zone (SMTZ) are indicated by the gray fields. (For interpretation of the references to colour in this figure legend, the reader is referred to the web version of this article.)

(Fig. 4 and Table 3). This implies that the active pockmarks B and D as well as the inactive pockmark E acted as sources of CH_4 to the seawater column. This is in agreement with the results of previous studies of CH_4 fluxes from pockmarks in the Baltic Sea (e.g., Bussmann and Suess, 1998; Idczak et al., 2020; Pimenov et al., 2010). However, in contrast to the studies by Bussmann and Suess (1998) in the Eckernförde Bay, and Pimenov et al. (2010) in the Gdansk Basin, (Fig. 1), CH_4 concentrations in the sea surface water (2 m) were elevated compared to the deeper water samples at all the pockmark site studied here (Fig. 4). This may result from the fact that the water columns above the pockmarks were stratified as indicated by the lower Cl^- concentrations measured at 2 m water depth compared to the Cl^- concentrations in 10 m water depth (Table 3). Obviously, a CH_4-enriched surface water layer, probably originating from river discharge, was encountered during the study in September 2019. The fact that CH_4 concentrations in the surface layer above the pockmarks were comparable to the CH_4 concentration at 2 m water depth at the offshore station J (Table 3) is line with the idea of a surface layer mainly affected by river discharge. The CH_4 bottom water concentrations measured during the seasonal study at the active pockmark site in Eckernförde Bay (Bussmann and Suess,1998) ranged from 0.011 (February 1999) to 0.441 µmol/L (December 1994) and were, thus, higher than the CH_4 concentrations at 10 m water depth (0.006 – 0.021 µmol/L) at the active pockmarks B and D but much lower than the CH_4 concentration in the bottom water (24.2 µmol/L) at the inactive pockmark E measured in September 2019. This indicates that CH_4 concentration gradients across the sediment–water interface at pockmark sites are highly variable in space and time. Therefore, any estimate of the overall input of CH_4 to the overlying water

column is associated with high uncertainty when neglecting the spatial–temporal variability of the CH_4 fluxes from pockmarks.

5.2. Microbial communities

Sediment in pockmark E can be considered "typical" for muddy sediments in the coastal Baltic Sea according to its microbial community structure, and the microbiological data largely concur with the sediment and porewater geochemistry. The high numbers of functional genes for sulfate reduction and methanogenesis agree with the high modelled reaction rates at pockmark E, compared to lower numbers of functional marker gene copies and reaction rates in pockmarks B and D. Furthermore, the archaeal and bacterial community in pockmark E resembles that of sediments from the nearby Pojo bay described in Myllykangas et al. (2020b). Archaeal taxa belonging to *Methanomicrobia* and *Thermoplasmata* as well as to *Woesearchaeota* were the most dominant groups in sediments of pockmark E as well as in Pojo Bay (Myllykangas et al., 2020b). Detection of the methanogenic community and higher numbers of methanogenesis marker gene *mcr*A correspond to high CH_4 concentrations in porewaters of the pockmark E, compared to the active pockmarks. The methanogenic community contains both hydrogenotrophs and aceticlastic methanogens. Woesearchaeota, a recently proposed archaeal phylum (Castelle et al., 2015) are defined as heterotrophs with metabolic deficiencies. Therefore, these organisms likely demand a partnering organism(s) or complementary existence of other microbes. A potential syntrophic relationship between methanogens and Woesearchaota has been suggested, as these organisms co-occur most often with *Methanobacteria* and *Methanomicrobia*, which were also found from pockmark E sediment (Liu et al., 2018). In addition to Woesearchaeota, Thermoplasmata complement the archaeal heterotrophic community in pockmark E.

Dominant bacteria in pockmark E were gammaproteobacteria, deltaproteobacterial sulfate reducers and *Bacteroidia* that in addition to corresponding to Baltic sea coastal sediments, also resemble surficial sediments of inactive pockmarks from Oslofjord, Norway (Haverkamp et al., 2014). Sulfate reducers (for example *Desulfubulbaceaea*) that were abundant in the sampled shallow sediments of pockmark E, have been detected elsewhere in Hanko cape sediment, where these have been shown to be resistant to hypoxic conditions (Sinkko et al., 2019). Sulfate reduction marker genes were present in order(s) of magnitude higher numbers in pockmark E compared to the other two pockmarks, again agreeing with the modelled high flux and sulfate reduction rates in the first $\sim$ 20 cm of pockmark E sediment. The detection of high numbers of both *mcr*A gene copies could indicate the presence of anaerobic methane oxidizing organisms (Hallam et al., 2003) in addition to methanogenesis, although only a small fraction of the archaeal community was representing those typical ANMEs (anaerobic methane-oxidizing archaea).

While the microbial community in pockmark E resembles other typical sediment communities in the pelagic Baltic Sea, the effect of SGD is clear in the pockmark B and especially in pockmark D sediment communities. Likely the groundwater advection obstructs the formation of SMTZ and thus limits the number of microbes involved in these processes. This could be due to a combination of low OM accumulation rates, low nutrient content of the groundwater or more oxygenated fluid seepage through the seafloor (Idczak et al., 2020). However, numerous nitrogen cycling organisms were detected in the active pockmarks. For example, OTUs affiliating with *Candidatus* Nitrosotalea were abundant in both pockmark D sediment and in groundwater from the observation well. The members of this candidate taxon have been described to be chemolithotrophic ammonia oxidizers (Lehtovirta-Morley et al., 2011, 2016; Prosser and Nicol, 2016). Interestingly, the two cultivated organisms of this lineage are obligate acidophiles (Prosser and Nicol, 2016). OTUs affiliating with another archaeal ammonia oxidizer *Nitrosoarchaeum* were detected in groundwater and both active pockmarks. *Nitrosoarchaeum* organisms are typical in aquatic environments with low salinity (Tolar et al., 2019), thus their abundance in groundwater and active pockmarks in our study is not surprising. Similarly, thaumarchaeal ammonia oxidizing archaea, which were dominating the seawater archaeal communities but also found in relatively high abundance in active pockmark sediments here, are major ammonia oxidizers in the oceans. *Nitrosopumilaceae* is especially dominant in oxygen minimum zones and the bathypelagic realm (Stahl and De La Torre, 2012; Muck et al., 2019).

Bacterial communities in pockmark D sediment differed from B and E with relatively high abundance of Nitrospira. These nitrifying bacteria are highly abundant, diverse and ubiquitous in natural ecosystems (Lücker et al., 2010). *Nitrospira* perform a critical second step of oxidation of nitrite to nitrate in nitrification, and some members of *Nitrospira* can perform complete nitrification from ammonia to nitrate (comammox)(Lücker et al., 2010; Koch et al., 2015; Koch et al., 2019). In the active pockmarks B and D therefore, a rather developed nitrogen cycle may exist that includes AOA converting ammonia to nitrite and secondly *Nitrospira*-like organisms oxidizing nitrite to nitrate. Efficient nitrogen cycling is especially important to ecosystems with limited amounts of substrates such as the active pockmarks in our case. The copy numbers of nitrogen cycling genes did not clearly reflect the concentrations of ammonium, with similar copy numbers for *amo*A at sites D and E (Fig. 6), but this might be due to the primer mismatches and unspecificity of the assay (Könneke et al., 2005). In addition, gene abundances are not to be used solely as a proxy for biogeochemical processes (Rocca et al., 2015).

The active pockmarks D and B appear to have the higher overall microbial density as well as higher functional gene copy numbers in the near-surface sediment, while in the inactive pockmark E has much higher copy numbers of all measured genes deeper in the sediment. As microbial activity and diversity hotspots are usually formed in the interfaces or mixing zones (McClain et al., 2003; Stegen et al., 2016), this can explain the higher copy numbers in the near-surface in active pockmarks. Namely, the physical forces, such as wave action, perturb the surface of the active

pockmarks mixing the fluffy organic substances on the sediment surface (see Supplementary Material, Fig. S1) into the first few centimeters of the sediment column (Huettel et al., 1996), thus providing more substrate for the microbial community compared to the deeper layers. These observations are confirmed by the reactive transport modeling results, which show that most of the reactions occur in the first few centimeters in the active pockmark sediments (Fig. 12).

Previous studies have shown that the freshwater and saline water mixing zone can be a diversity hotspot and induce the growth of rare taxa (Rocca et al., 2020; Ruiz-González et al., 2021 and references therein). However, the most diverse communities in our study were detected from the inactive pockmark E, where higher and more varied organic matter content likely plays a role in diversifying microbial communities (Delgado-Baquerizo et al., 2016). Specifically, the microbial community requires diverse abilities to degrade the versatile and likely more recalcitrant organic material ending up into the inactive pockmark sediment.

Based on our results on the microbial community composition in active and inactive pockmarks and the literature of the prevalent microbial communities hosted by the seafloor in the coastal Baltic sea, we can conclude that focused SGD at pockmark localities change the local seafloor microbial community composition. This can mean activation of rare biosphere but also inactivation of other members of the community, thus impacting the ecosystem processes (Allison and Martiny 2008, Ruiz-González et al., 2021 and references therein). However, a part of the community appears to be resistant to the environmental change, and when groundwater flow seizes and the pockmark turns into an inactive one, the microbial community will alter again towards the typical seafloor community. Therefore, although the microbial community structure changes, it appears to be able to perform as the original one, thus staying functionally redundant (Allison and Martiny, 2008).

5.3. Impact of SGD on biogeochemical processes and microbial community in the coastal zone

Discharge rates calculated for pockmarks B and D based on porewater Cl^- profiles are 0.02 cm d^{-1} and 0.31 cm d^{-1}, respectively (Fig. 5). These values are in general agreement with the simulated average discharge rates from the groundwater flow model of 0.22 cm d^{-1} (range 0.0–1.21 cm d^{-1}) and 0.28 cm d^{-1} (range 0.0–1.60 cm d^{-1}) for fine sand in the pockmark area for autumn 2017 and spring 2020, respectively (Luoma et al., 2021). The discharge rates (range 0.4–1.2 cm d^{-1}) estimated by ^{222}Rn measurements in May 2018 are higher but those rates were measured 1 m above pockmark bottom and integrate SGD over a larger area in each pockmark, with potential influence from the neighbouring pockmarks (Virtasalo et al., 2019). Unpublished underwater videos show patchy water discharge from the pockmark sediment surface. SGD rates similar to those estimated for pockmarks B and D have been calculated for pockmarks in Eckernförde Bay applying the same methodology (mean 0.05 cm d^{-1}, maximum 0.9 cm d^{-1}, Schlüter et al., 2004).

Our results demonstrate a strong impact of SGD on both biogeochemical reaction rates and the microbial community composition responsible for the reactions. Pockmark D shows the impacts most clearly, with high rates of vertical advection compressing the reactants available for biogeochemical reactions into a narrow zone at the sediment surface, leading to a focusing of the microbial community into the uppermost centimeters of the sediment column. Coupled with the physical effect of SGD reducing the accumulation of OM, this also results in the absence of a SMTZ at this site. This differs from other pockmark sites in the Baltic Sea (Schlüter et al., 2004; Idczak et al., 2020), suggesting that the groundwater impact on biogeochemistry is more pronounced at our study location.

With only a few published studies on microbiology at the groundwater–seawater mixing zones in coastal aquifers and especially in pockmarks associated with SGD, commonalities in microbial community structure in these systems are still the topic of active research (Ruiz-González et al., 2021). However, the microbial community structure in the active pockmarks B and D appears comparable to other SGD sites (Idczak et al., 2020; Adyasari et al., 2019, 2020). Gamma- and Alphaproteobacteria have been reported as the typical phyla in bacterial communities, similarly to our study. Salinity is identified as the most important factor in shaping the microbial community in oxic Baltic Sea sediments (Klier et al., 2018), hence the influence of groundwater on the communities at sites B, D, and E is partly expressed through contrasting salinity in the porewaters. Adyasari et al. (2019) reported *Burkholderia*-affiliating OTUs specifically representing fresh groundwater species. Similarly, in groundwater and the groundwater-dominated pockmark D, the proportions of *Burkholderiales* were relatively high. Salinity also has an effect on ammonia oxidizing microbial communities. According to Santoro et al. (2008), the bacterial dominance of the ammonia-oxidizing community declines with decreasing salinity. Similarly, in our study the abundance of ammonia oxidizing bacteria was lower in pockmark D with 0 salinity compared to pockmarks E and B where salinity was up to 6.

The inactive pockmark E displays a sedimentation rate several times higher than those documented for nearby organic-rich mud seafloor areas (0.3–0.5 cm yr^{-1}; Jokinen et al., 2020). In contrast, active pockmarks B and D have not had substantial deposition in the recent past due to strong SGD. This pronounced change in sedimentation rate upon deactivation of the pockmark E is important for understanding solute fluxes at the sediment–water interface at different stages of the life cycle of these systems. Since sediment deposition is the key control of OM delivery to the seafloor, and locally elevated deposition rates are expected to impact biogeochemical processes and microbial community composition in pockmark sediments (Idczak et al., 2020; O'Reilly et al., 2021) pockmark E expectedly displays far higher concentrations and fluxes of metabolites and CH_4 at the sediment–water interface than the active pockmarks. Moreover, the exceptionally high sedimentation rates in pockmark E suggest that inactive pockmarks

may act as a localized sediment trap due to their bathymetric configuration. This raises the possibility that inactive pockmarks in this system act as a hotspot for diffusive nutrient and gas fluxes to bottom waters, in contrast to the active pockmarks where solute fluxes are comparatively low despite high rates of advection (Table 5). These results highlight the importance of redox-dependent processes taking place in subterranean estuaries on the development of the chemical gradients at the fresh-salt water interface (Beck et al., 2007; Moosdorf et al., 2021). However, two further pertinent observations follow from this. Firstly, the diffusive fluxes of nutrients and CH_4 observed at inactive pockmarks result from OM cycling that may be considered "internal" to the marine system, because the primary source of the decaying OM in the sediment column is settling plankton detritus, while nutrient fluxes from SGD, even if small, must be considered as external inputs. Second, persistently inactive pockmarks are expected to fill in over time (Pau and Hammer, 2013), especially in coastal areas where sediment deposition predominantly takes place from lateral near-bottom sediment transport (Virtasalo et al., 2014; Jokinen et al., 2015). Thus, it is likely that the eventual fate of an inactive pockmark is a setting with a similar sedimentation regime to the surrounding seafloor areas. The overall effect of the SGD-related pockmarks on solute fluxes at any point in time is expected to be a function of the number of individual pockmarks, the rate of SGD, and the ratio of active to inactive pockmarks in the system as a whole.

6. CONCLUSIONS

This present study investigates how SGD impacts on biogeochemical processes and microbial community structure in a coastal sea area. The impacted active sites were compared to the diagenesis-dominated reference site.

SGD rates calculated from porewater Cl^- profiles show strong groundwater influence for pockmarks B and D. Their porewater systems are dominated by groundwater advection, which pushes the reactants available for biogeochemical reactions into a narrow zone at the sediment surface and leads to a focusing of the microbial activity into the top part of the sediment column. The advection further reduces the accumulation of OM in the surface sediments, resulting in the absence of SMTZ in these pockmarks. Reactive transport modelling consequently estimates low depth-integrated fluxes of SO_4^{2-}, CH_4, NH_4^+, DIC at pockmarks B and D, and further suggests Fe-AOM to contribute to methane oxidation in these pockmarks. Groundwater influence is visible in the microbial community structure of the active pockmarks, in which notable populations of ammonia-oxidizing archaea and nitrifying bacteria are of predominantly groundwater origin.

The lack of SGD permits rapid deposition of organic-rich mud in the currently inactive pockmark E. The porewater system at this site is dominated by diffusion, leading to orders of magnitude higher concentrations of CH_4, NH_4^+, DIC at depth compared to pockmarks B and D. The biogeochemical environment in pockmark E resembles typical organic-rich mud seafloor in the area, with sulfate reduction and methanogenesis as the dominant organic matter remineralization pathways. Reactive transport modelling shows that S-AOM occurs in the pockmark at a similar depth range to organoclastic sulfate reduction, and accounts for approximately 10% of total sulfate consumption at this depth. The presence of S-AOM is supported by porewater DIC, SO_4^{2-} and $\delta^{13}C$-DIC signatures. Methanogens are relatively more abundant in the archaeal community in pockmark E compared to active pockmarks, whereas sulfate reducers dominate the bacterial community. Although the depth-integrated fluxes of SO_4^{2-}, CH_4, NH_4, DIC at pockmark E are orders of magnitude higher compared to pockmarks B and D, processes at this site are driven by recent OM accumulation and thus represent internal recycling in the coastal sea. In contrast, processes at the active pockmarks B and D are partially mediated by SGD inputs and therefore effluxes of dissolved substances across the sediment–water interface must be considered to be influenced by external inputs to the sea.

DECLARATION OF COMPETING INTEREST

The authors declare that they have no known competing financial interests or personal relationships that could have appeared to influence the work reported in this paper.

ACKNOWLEDGEMENTS

This work resulted from the BONUS SEAMOUNT project supported by BONUS (Art 185), funded jointly by the EU and the Academy of Finland (grant no. 311983). CV was supported by DAAD via a PhD stipend (project no. 57381412). This study was conducted within the framework of the Research Training Group 'Baltic TRANSCOAST' funded by the DFG (Deutsche Forschungsgemeinschaft) under grant number GRK 2000 (www.baltic-transcoast.uni-rostock.de). This is Baltic TRANSCOAST publication no. GRK2000/0055. TJ acknowledges support from Academy Research Fellowship 317684. This study has utilized research infrastructure facilities provided by FINMARI (Finnish Marine Research Infrastructure network). Annette Kock (GEOMAR Helmholtz Centre for Ocean Research Kiel) is acknowledged for her support on the CH_4 water column measurements. Malin Bomberg and Päivi Kinnunen (VTT Technical Research Centre) are thanked for the opportunity to perform qPCR in their facilities. CV and MB wish to thank Iris Schmiedinger for expert laboratory and mass spectrometric support. Expert support from the captain and the crew of R/V Geomari and the people who further assisted in the fieldwork is gratefully acknowledged.

APPENDIX A. SUPPLEMENTARY MATERIAL

Supplementary material to this article can be found online at https://doi.org/10.1016/j.gca.2022.06.040.

REFERENCES

Adyasari D., Hassenrück C., Oehler T., Sabdaningsih A. and Moosdorf N. (2019) Microbial community structure associated with submarine groundwater discharge in northern Java (Indonesia). *Sci. Total Environ.* **689**, 590–601.

Adyasari D., Hassenrück C., Montiel D. and Dimova N. (2020) Microbial community composition across a coastal hydrological system affected by submarine groundwater discharge (SGD). *PLoS ONE* **15**, e0235235.

Allison S. D. and Martiny J. B. H. (2008) Resistance, resilience, and redundancy in microbial communities. *Proc. Natl. Acad. Sci. U. S. A.* **105**, 11512–11519.

Bange H. W., Bergmann K., Hansen H. P., Kock A., Koppe R., Malien F. and Ostrau C. (2010) Dissolved methane during hypoxic events at the Boknis Eck Time Series Station (Eckernförde Bay, SW Baltic Sea). *Biogeosciences* **7**, 1279–1284.

Beck A. J., Tsukamoto Y., Tovar-Sanchez A., Huerta-Diaz M., Bokuniewicz H. J. and Sañudo-Wilhelmy S. A. (2007) Importance of Geochemical Transformations in Determining Submarine Groundwater Discharge-Derived Trace Metal and Nutrient Fluxes. *Appl. Geochem.* **22**, 477–490.

Berg P., Rysgaard S. and Thamdrup B. (2003) Dynamic modeling of early diagenesis and nutrient cycling. A case study in an Arctic marine sediment. *Am. J. Sci.* **303**, 905–955.

Bernard R. J., Mortazavi B., Wang L., Ortmann A. C., MacIntyre H. and Burnett W. C. (2014) Benthic nutrient fluxes and limited denitrification in a sub-tropical groundwater-influenced coastal lagoon. *Mar. Ecol. Prog. Ser.* **504**, 13–26.

Berner R. A. (1970) Sedimentary pyrite formation. *Am. J. Sci.* **268**, 1–23.

Blott S. J. and Pye K. (2012) Particle size scales and classification of sediment types based on particle size distributions: review and recommended procedures. *Sedimentology* **59**, 2071–2096.

Böttcher M. E., Mallast U., Massmann G., Moosdorf N., Müller-Petke M. and Waska H. (2020) Coastal-Groundwater interfaces (submarine groundwater discharge). In *Ecohydrological Interfaces* (ed. S. Krause). Wiley, USA.

Boudreau B. P. (1987) A steady-state diagenetic model for dissolved carbonate species and pH in the porewaters of oxic and suboxic sediments. *Geochim. Cosmochim. Acta* **51**, 1985–1996.

Boudreau B. P. (1996) The diffusive tortuosity of fine-grained unlithified sediments. *Geochim. Cosmochim. Acta* **60**, 3139–3142.

Boudreau B. P. (1997) *Diagenetic Models and their Implementation: Modelling Transport and Reactions in Aquatic Sediments*. Springer-Verlag, Heidelberg.

Boudreau B. P., Meysman F. J. R. and Middelburg J. J. (2004) Multicomponent ionic diffusion in porewaters: coulombic effects revisited. *Earth Planet. Sci. Lett.* **222**, 653–666.

Brand W. A. and Coplen T. B. (2012) Stable Isotope Delts: Tiny, yet Robust Signatures in Nature. *Isotopes Environ. Health Stud.* **48**, 393–409.

Brüchert V. (1998) Early diagenesis of sulfur in estuarine sediments: the role of sedimentary humic and fulvic acids. *Geochim. Cosmochim. Acta* **62**, 1567–1586.

Bussmann I. and Suess E. (1998) Groundwater seepage in Eckernförde Bay (Western Baltic Sea): Effect on methane and salinity distribution of the water column. *Continen. Shelf Res.* **18**, 1795–1806.

Castelle C. J., Wrighton K. C., Thomas B. C., Hug L. A., Brown C. T., Wilkins M. J., Frischkorn K. R., Tringe S. G., Singh A., Markillie L. M., Taylor R. C., Williams K. H. and Banfield J. F. (2015) Genomic expansion of domain archaea highlights roles for organisms from new phyla in anaerobic carbon cycling. *Curr. Biol.* **25**, 690–701.

Cho H.-M., Kim G., Kwon E. Y., Moosdorf N., Garcia-Orellana J. and Santos I. R. (2018) Radium tracing nutrient inputs through submarine groundwater discharge in the global ocean. *Sci. Rep.* **8**, 2439.

Church T. M. (1996) An underground for the water cycle. *Nature* **380**, 579–580.

Delgado-Baquerizo M., Maestre F. T., Reich P. B., Jeffries T. C., Gaitan J. J., Encinar D., Berdugo M., Campbell C. D. and Singh B. K. (2016) Microbial diversity drives multifunctionality in terrestrial ecosystems. *Nat. Commun.* **7**, 1–8.

Donis D., Janssen F., Liu B., Wenzhöferö F., Dellwig O., Escher P., Spitzy A. and Böttcher M. E. (2017) Biogeochemical Impact of Submarine Groundwater Discharge on Coastal Surface Sands of the Southern Baltic Sea. *Est., Coast. Shelf Sci.* **189**, 131–142.

Egger M., Lenstra W., Jong D., Meysman F. J., Saoart C. J., Van der Veen C., Rockmann T., Gonzales S. and Slomp C. P. (2016b) Rapid sediment accumulation results in high methane effluxes from coastal sediments. *PLos One* **11**.

Egger M., Kraal P., Jilbert T., Sulu-Gambari F., Sapart C. J., Rockmann T. and Slomp C. P. (2016a) Anaerobic oxidation of methane alters sediment records of sulfur, iron and phosphorus in the Black Sea. *Biogeosciences* **13**, 5333–5355.

Egger M., Hagens M., Sapart C. J., Dijkstra N., van Helmond N. A. G. M., Mogollón J. M., Risgaard-Petersen N., van der Veen C., Kasten S., Riedinger N., Böttcher M. E., Röckmann T., Jørgensen B. B. and Slomp C. P. (2017) Iron oxide reduction in methane-rich deep Baltic Sea sediments. *Geochim. Cosmochim. Acta* **207**, 256–276.

Folk R. L. and Ward W. C. (1957) Brazos river bar: a study in the significance of grain size parameters. *J. Sediment. Petrol.* **27**, 3–26.

Froelich P. N., Klinkhammer G. P., Bender M. L., Luedtke N. A., Heath G. R., Cullen D., Dauphin P., Hammond D., Hartman B. and Maynard V. (1979) Early oxidation of organic matter in pelagic sediments of the eastern equatorial Atlantic: suboxic diagenesis. *Geochim. Cosmochim. Acta* **43**, 1075e1090.

Fyfe G. J. (1990) The effect of water depth on ice-proximal glaciolacustrine sedimentation: Salpausselkä I, southern Finland. *Boreas* **19**, 147–164.

Gantner S., Andersson A. F., Alonso-Sáez L. and Bertilsson S. (2011) Novel primers for 16S rRNA-based archaeal community analyses in environmental samples. *J. Microbiol. Methods* **84**, 12–18.

Giambalvo E. R., Steefel C. I., Fisher A. T., Rosenberg N. D. and Wheat C. G. (2002) Effect of fluid-sediment reaction on hydrothermal fluxes of major elements, eastern flank of the Juan de Fuca Ridge. *Geochim. Cosmochim. Acta* **66**, 1739–1757.

Grasshoff K., Kremling K. and Ehrhardt M. (2009) *Methods of Seawater Analysis*. John Wiley & Sons, Weinheim.

Hall G. E. M., Vaive J. E., Beer R. and Hoashi M. (1996) Selective leaches revisited, with emphasis on the amorphous Fe oxyhydroxide phase extraction. *J. Geochem. Explor.* **56**, 59–78.

Hallam S. J., Girguis P. R., Preston C. M., Richardson P. M. and DeLong E. F. (2003) Identification of methyl coenzyme M reductase A (mcrA) genes associated with methane-oxidizing archaea. *Appl. Environ. Microbiol.* **69**, 5483–5491.

Hammer Ø., Harper D. A. T. and Ryan P. D. (2001) Past: Paleontological Statistics Software Package for education and data analysis. *Paleontología Electrónica* **4**, 1–9 http://palaeo-electronica.org/2001_1/past/issue1_01.html.

Haverkamp T. H. A., Hammer Ø. and Jakobsen K. S. (2014) Linking Geology and Microbiology: Inactive Pockmarks Affect Sediment Microbial Community Structure. *PLoS ONE* **9**, e85990.

Hoffmann J. J. L., Schneider von Deimling J., Schröder J. F., Schmidt M., Held P., Crutchley G. J., Scholten J. and Gorman A. R. (2020) Complex eyed pockmarks and submarine groundwater discharge revealed by acoustic data and sediment cores in

Eckernförde Bay, SW Baltic Sea. *Geochem. Geophys. Geosyst.* **21**, e2019GC008825.

Holby O. and Evans S. (1996) The vertical distribution of Chernobyl-derived radionuclides in a Baltic Sea sediment. *J. Environ. Radioactiv.* **33**, 129–145.

Hu Y., Feng D., Liang Q., Xia Z., Linying C. and Chen D. (2015) Impact of anaerobic oxidation of methane on the geochemical cycle of redox-sensitive elements at cold-seep sites of the northern South China Sea. *Deep-Sea Res. Part II-Top. Stud. Oceanogr.* **122**, 84–94.

Huettel M., Ziebis W. and Forster S. (1996) Flow-induced uptake of particulate matter in permeable sediments. *Limnol. Oceanogr.* **4l**, 309–322.

Idczak J., Brodecka-Goluch A., Łukawska-Matuszewska K., Graca B., Gorska N., Klusek Z., Pezacki P. D. and Bolałek J. (2020) A geophysical, geochemical and microbiological study of a newly discovered pockmark with active gas seepage and submarine groundwater discharge (MET1-BH, central Gulf of Gdańsk, southern Baltic Sea). *Sci. Total Environ.* **742**, 140306.

Jensen J. B., Kuijpers A., Bennike O., Laier T. and Werner F. (2002) New geological aspects for freshwater seepage and formation in Eckernförde Bay, western Baltic. *Cont. Shelf Res.* **22**, 2159–2173.

Jilbert T., Asmala E., Schroder C., Tiihonen R., Myllykangas J., Virtasalo J. J., Kotilainen A., Peltola P., Ekholm P. and Hietanen S. (2018) Impacts of flocculation on the distribution and diagenesis of iron in boreal estuarine sediments. *Biogeosciences* **15**, 1243–1271.

Jilbert T., Cowie G., Lintumäki L., Jokinen S., Asmala E., Sun X., Mörth C.-M., Norkko A. and Humborg C. (2021) Anthropogenic inputs of terrestrial organic matter influence carbon loading and methanogenesis in coastal Baltic Sea sediments. *Front. Earth Sci.* **9**.

Johannes R. E. (1980) The ecological significance of the submarine groundwater discharge. *Mar. Ecol. Prog. Ser.* **3**, 365–373.

Jokinen S. A., Virtasalo J. J., Kotilainen A. T. and Saarinen T. (2015) Varve microfabric record of seasonal sedimentation and bottom flow-modulated mud deposition in the coastal northern Baltic Sea. *Mar. Geol.* **366**, 79–96.

Jokinen S. A., Jilbert T., Tiihonen-Filppula R. and Koho K. (2020) Terrestrial organic matter input drives sedimentary trace metal sequestration in a human-impacted boreal estuary. *Sci. Total Environ.* **717**, 137047.

Jørgensen B. B. (1978) A comparison of methods for the quantification of bacterial sulfate reduction in coastal marine sediments, II. Calculations from mathematical models. *Geomicrobiol. J.* **1**, 29–51.

Jørgensen B. B., Beulig F., Egger M., Petro C., Scholtze C. and Røy H. (2019) Organoclastic sulfate reduction in the sulfate-methane transition of marine sediments. *Geochim. Cosmochim. Acta* **254**, 231–325.

Jørgensen B. B. and Kasten S. (2006) Sulfur cycling and methane oxidation. In *Marine Geochemistry* (eds. H. D. Schulz and M. Zabel). Springer-Verlag, Berlin Heidelberg, pp. 271–309.

Kakkuri J. (2012) Fennoscandian land uplift: past, present and future. In *From the Earth's Core to Outer Space* (ed. I. Haapala). Springer-Verlag, Berlin Heidelberg, pp. 127–136.

Kastner M., Claypool G. and Robertson G. (2008) Geochemical constraints on the origin of the pore fluids and gas hydrate distribution at Atwater Valley and Keathley Canyon, northern Gulf of Mexico. *Mar. Pet. Geol.* **25**, 860–872.

Kielosto S., Kukkonen M., Stén C.-G. and Backman B. (1996) *Hangon ja Perniön kartta-alueiden maaperä. Summary: Quaternary deposits in the Hanko and Perniö map-sheet areas, Geological map of Finland 1 : 100 000. Explanation to the maps of Quaternary deposits, sheets 2011 and 2012*. Geological Survey of Finland, Espoo.

Kisand V., Cuadros R. and Wikner J. (2002) Phylogeny of culturable estuarine bacteria catabolizing riverine organic matter in the northern Baltic Sea. *Appl. Environ. Microbiol.* **68**, 379–388.

Klaminder J., Appleby P., Crook P. and Renberg I. (2012) Postdeposition diffusion of ^{137}Cs in lake sediment: implications for radiocaesium dating. *Sedimentology* **59**, 2259–2267.

Klier J., Dellwig O., Leipe T., Jürgens K. and Herlemann D. P. R. (2018) Benthic Bacterial Community Composition in the Oligohaline-Marine Transition of Surface Sediments in the Baltic Sea Based on rRNA Analysis Available at:. *Front. Microbiol.* **9**, 236 http://journal.frontiersin.org/article/10.3389/fmicb.2018.00236/full.

Knee K. and Paytan A. (2011) 4.08 submarine groundwater discharge: a source of nutrients, metals, and pollutants to the coastal ocean. *Treatise Estuar. Coast. Sci.* **4**, 205–233.

Koch H., Lücker S., Albertsen M., Kitzinger K., Herbold C., Spieck E., Nielsen P. H., Wagner M. and Daims H. (2015) Expanded metabolic versatility of ubiquitous nitrite-oxidizing bacteria from the genus Nitrospira. *Proc. Natl. Acad. Sci. U. S. A* **112**, 11371–11376.

Koch H., van Kessel M. A. H. J. and Lücker S. (2019) Complete nitrification: insights into the ecophysiology of comammox Nitrospira. *Appl. Microbiol. Biotechnol.* **103**, 177–189.

Könneke M., Bernhard A. E., de la Torre J. R., Walker C. B., Waterbury J. B. and Stahl D. (2005) Isolation of an autotrophic ammonia-oxidizing marine archaeon. *Nature* **437**, 543–546.

Kotwicki L., Grzelak K., Czub M., Dellwig O., Gentz T., Szymczycha B. and Böttcher M. E. (2014) Submarine groundwater discharge to the Baltic coastal zone: Impacts on the meiofaunal community. *J. Mar. Syst.* **129**, 118–126.

Kozich J. J., Westcott S. L., Baxter N. T., Highlander S. K. and Schloss P. D. (2013) Development of a dual-index sequencing strategy and curation pipeline for analyzing amplicon sequence data on the Miseq Illumina sequencing platform. *Appl. Environ. Microbiol.* **79**, 5112–5120.

Kujansuu R., Uusinoka R., Herola E. and Sten C.-G. (1993) *Tammisaaren kartta-alueen maaperä. Summary Quaternary deposits in the Tammisaari map-sheet area, Geological map of Finland 1 : 100 000. Explanation to the maps of Quaternary deposits, sheet 2014*. Geological Survey of Finland, Espoo.

Kumblad L. and Bradshaw C. (2008) *Element composition of biota, water and sediment in the Forsmark area, Baltic Sea: concentrations, bioconcentration factors and partitioning coefficients (Kd) of 48 elements*. Swedish Nuclear Fuel and Waste Management Co, Stockholm.

Lecher A. L. and Mackey K. R. M. (2018) Synthesizing the Effects of Submarine Groundwater Discharge on Marine Biota. *Hydrology* **5**, 60.

Lee E., Shin D., Hyun S. P., Ko K. S., Moon H. S., Koh D. C., Ha K. and Kim B. Y. (2017) Periodic change in coastal microbial community structure associated with submarine groundwater discharge and tidal fluctuation. *Limnol. Oceanogr.* **62**, 437–451.

Lehtovirta-Morley L. E., Stoecker K., Vilcinskas A., Prosser J. I. and Nicol G. W. (2011) Cultivation of an obligate acidophilic ammonia oxidizer from a nitrifying acid soil. *Proc. Natl. Acad. Sci. U. S. A.* **108**, 15892–15897.

Lehtovirta-Morley L. E., Sayavedra-Soto L. A., Gallois N., Schouten S., Stein L. Y., Prosser J. I. and Nicol G. W. (2016) Identifying Potential Mechanisms Enabling Acidophily in the Ammonia-Oxidizing Archaeon *Candidatus Nitrosotalea devanaterra*. *Appl. Environ. Microbiol.* **82**, 2608–2619.

Liu X., Li M., Castelle C. J., Probst A. J., Zhou Z., Pan J., Liu Y., Banfield J. F. and Gu J.-D. (2018) Insights into the ecology,

evolution, and metabolism of the widespread Woesearchaeotal lineages Available at:. *Microbiome* **6**, 102 https://microbiomejournal.biomedcentral.com/articles/10.1186/s40168-018-0488-2.

Lücker S., Wagner M., Maixner F., Pelletier E., Koch H., Vacherie B., Rattei T., Damsté J. S. S., Spieck E., Le Paslier D. and Daims H. (2010) A Nitrospira metagenome illuminates the physiology and evolution of globally important nitrite-oxidizing bacteria. *Proc. Natl. Acad. Sci. U. S. A.* **107**, 13479–13484.

Luijendijk E., Gleeson T. and Moosdorf N. (2020) Fresh groundwater discharge insignificant for the world's oceans but important for coastal ecosystems. *Nat. Commun.* **11**, 1260.

Luoma S., Majaniemi J., Pullinen A., Mursu J. and Virtasalo J. J. (2021) Geological and groundwater flow model of a submarine groundwater discharge site at Hanko (Finland), northern Baltic Sea. *Hydrogeol. J.* **29**, 1279–1297.

McClain M. E., Boyer E. W., Dent C. L., Gergel S. E., Grimm N. B., Groffman P. M., Hart S. C., Harvey J. W., Johnston C. A., Mayorga E., McDowell W. H. and Pinay G. (2003) Biogeochemical Hot Spots and Hot Moments at the Interface of Terrestrial and Aquatic Ecosystems. *Ecosystems* **6**, 301–312.

Merkouriadi I. and Leppäranta M. (2014) Long-term analysis of hydrography and sea-ice data in Tvärminne, Gulf of Finland, Baltic Sea. *Clim. Change* **124**, 849–859.

Meysman F. J. R., Boudreau B. P. and Middelburg J. J. (2005) Modeling reactive transport in sediments subject to bioturbation and compaction. *Geochim. Cosmochim. Acta* **69**, 3601–3617.

Middelburg J. J. (1989) A simple rate model for organic matter decomposition in marine sediments. *Geochim. Cosmochim. Acta* **53**, 1577–1581.

Miller C. M., Dickens G. R., Jakobsson M., Johansson C., Koshurnikov A., O'Regan M., Muschitiello F., Stranne C. and Morth C. (2017) Pore water geochemistry along continental slopes north of the East Siberian Sea: inference of low methane concentrations. *Biogeosciences* **14**, 2929–2953.

Mogollón J. M., Dale A. W., Jensen J. B., Schlüter M. and Regnier P. (2013) A method for the calculation of anaerobic oxidation of methane rates across regional scales: an example from the Belt Seas and The Sound (North Sea-Baltic Sea transition). *Geo-Mar. Lett.* **33**, 299–310.

Moodley L., Middelburg J. J., Herman P. M. J., Soetaert K. and de Lange G. J. (2005) Oxygenation and organic-matter preservation in marine sediments: Direct experimental evidence from ancient organic carbon–rich deposits. *Geology* **33**, 889–892.

Moore W. S. (2010) The effect of submarine groundwater discharge on the ocean. *Annu. Rev. Mar. Sci.* **2**, 59–88.

Moosdorf N., Böttcher M. E., Adyasari D., Erkul E., Gilfedder B., Greskowiak J., Jenner A.-K., Kotwicki L., Massmann G., Petke M. M., Oehler T., Post V., Prien R., Scholten J., Siemon B., von Ahn C. M. E., Walther M., Waska H., Wunderlich T. and Mallast U. (2021) A State-Of-The-Art Perspective on the Characterization of Subterranean Estuaries at the Regional Scale. *Front. Earth Sci.* **9**, 601293.

Muck S., De Corte D., Clifford E. L., Bayer B., Herndl G. J. and Sintes E. (2019) Niche Differentiation of Aerobic and Anaerobic Ammonia Oxidizers in a High Latitude Deep Oxygen Minimum Zone Available at:. *Front. Microbiol.* **10**, 2141 https://www.frontiersin.org/article/10.3389/fmicb.2019.02141/full.

Muniruzzaman M. and Rolle M. (2015) Impact of multicomponent ionic transport on pH fronts propagation in saturated porous media. *Water Resour. Res.* **51**, 6739–6755.

Muniruzzaman M. and Rolle M. (2017) Experimental investigation of the impact of compound-specific dispersion and electrostatic interactions on transient transport and solute breakthrough. *Water Resour. Res.* **53**, 1189–1209.

Muniruzzaman M., Haberer C. M., Grathwohl P. and Rolle M. (2014) Multicomponent ionic dispersion during transport of electrolytes in heterogeneous porous media: Experiments and model-based interpretation. *Geochim. Cosmochim. Acta* **141**, 656–669.

Myllykangas J., Jilbert T., Jakobs G., Rehder G., Werner J. and Hietanen S. (2017) Effects of the 2014 major Baltic inflow on methane and nitrous oxide dynamics in the water column of the central Baltic Sea. *Earth Syst. Dyn.* **8**, 817–826.

Myllykangas J., Hietanen S. and Jilbert T. (2020a) Legacy effects of eutrophication on modern methane dynamics in a boreal estuary. *Estuaries Coasts* **43**, 189–206.

Myllykangas J. P., Rissanen A. J., Hietanen S. and Jilbert T. (2020b) Influence of electron acceptor availability and microbial community structure on sedimentary methane oxidation in a boreal estuary. *Biogeochemistry* **148**, 291–309.

O'Reilly S. S., Jordan S. F., Monteys X., Simpson A. J., Allen C. C. R., Szpak M. T., Murphy B. T., McCarron S. G., Soong R., Wu B., Jenne A., Grey A. and Kelleher B. P. (2021) Production of methane and gaseous compounds by surface microbial activity in a small pockmark field, Dunmanus Bay, Ireland. *Estuar. Coast. Shelf Sci.* **255**, 107340.

Oehler T., Ramasamy M., George M. E., Babu S. D. S., Dähnke K., Ankele M., Böttcher M. E., Santos I. R. and Moosdorf N. (2021) Tropical beaches attenuate groundwater nitrogen pollution flowing to the ocean. *Environ. Sci. Technol.* **55**, 8432–8438.

Ojala A. E. K., Luoto T. P. and Virtasalo J. J. (2017) Establishing a high-resolution surface sediment chronology with multiple dating methods – testing ^{137}Cs determination with Nurmijärvi clastic-biogenic varves. *Quat. Geochronol.* **37**, 32–41.

Passier H. F., Böttcher M. E. and Lange G. J. D. (1999) Sulphur Enrichment in Organic Matter of Eastern Mediterranean Sapropels: A Study of Sulphur Isotope Partitioning. *Aquat. Geochem.* **5**, 99–118.

Pau M. and Hammer Ø. (2013) Sediment mapping and long-term monitoring of currents and sediment fluxes in pockmarks in the Oslofjord, Norway. *Mar. Geol.* **346**, 262–273.

Penttilä A., Slade E. M., Simojoki A., Riutta T., Minkkinen K. and Roslin T. (2013) Quantifying beetle-mediated effects on gas fluxes from dung pats. *PLoS One* **8**.

Pimenov N. V., Ulyanova M. O., Kanapatsky T. A., Veslopolova E. F., Sigalevich P. A. and Sivkov V. V. (2010) Microbially mediated methane and sulfur cycling in pockmark sediments of the Gdansk Basin, Baltic Sea. *Geo-Marine Letters* **30**, 439–448.

Pirinen P., Simola H., Aalto J., Kaukoranta J.-P., Karlsson P. and Ruuhela R. (2012) *Climatological Statistics of Finland 1981–2010*. Finnish Meteorological Institute, Helsinki.

Prosser J. I. and Nicol G. W. (2016) *Candidatus* Nitrosotalea. In *Bergey's Manual of Systematics of Archaea and Bacteria* (ed. W. B. Whitman). Wiley, Hoboken, New Jersey, pp. 1–7.

Reed D. C., Slomp C. P. and Gustafsson B. G. (2011a) Sedimentary phosphorus dynamics and the evolution of bottom-water hypoxia: A coupled benthic-pelagic model of a coastal system. *Limnol. Oceanogr.* **56**, 1075–1092.

Reed D. C., Slomp C. P. and de Lange G. J. (2011b) A quantitative reconstruction of organic matter and nutrient diagenesis in Mediterranean Sea sediments over the Holocene. *Geochim. Cosmochim. Acta.* **75**, 5540–5558.

Rocca J. D., Simonin M., Bernhardt E. S., Washburne A. D. and Wright J. P. (2020) Rare microbial taxa emerge when communities collide: freshwater and marine microbiome responses to experimental mixing. *Ecology* **101**, [Accessed November 4, 2021].

Rocca J. D., Hall E. K., Lennon J. T., Evans S. E., Waldrop M. P., Cotner J. B., Nemergut D. R., Graham E. B. and Wallenstein M. D. (2015) Relationships between protein-encoding gene abundance and corresponding process are commonly assumed yet rarely observed. *ISME J.* **9**, 1693–1699.

Rolle M., Muniruzzaman M., Haberer C. M. and Grathwohl P. (2013) Coulombic effects in advection-dominated transport of electrolytes in porous media: Multicomponent ionic dispersion. *Geochim. Cosmochim. Acta* **120**, 195–205.

Rolle M., Sprocati R., Masi M., Jin B. and Muniruzzaman M. (2018) Nernst-Planck-based description of transport, Coulombic interactions, and geochemical reactions in porous media: Modeling approach and benchmark experiments. *Water Resour Res.* **54**, 3176–3195.

Rooze J., Egger M., Tsandev I. and Slomp C. P. (2016) Iron-dependent anaerobic oxidation of methane in coastal surface sediments: Potential controls and impact. *Limnol. Oceanogr.* **61**, S267–S282.

Ruiz-González C., Rodellas V. and Garcia-Orellana J. (2021) The microbial dimension of submarine groundwater discharge: current challenges and future directions. *FEMS Microbiol. Rev.* **45**, 1–25.

Saarnisto M. and Saarinen T. (2001) Deglaciation chronology of the Scandinavian Ice Sheet from the Lake Onega Basin to the Salpausselkä end moraines. *Global Planet. Change* **31**, 387–405.

Santoro A. E., Francis C. A., de Sieyes N. R. and Boehm A. B. (2008) Shifts in the relative abundance of ammonia-oxidizing bacteria and archaea across physicochemical gradients in a subterranean estuary. *Environ. Microbiol.* **10**, 1068–1079.

Santos I. R., Chen X., Lecher A. L., Sawyer A. H., Moosdorf N., Rodellas V., Tamborski J., Cho H.-M., Dimova N., Sugimoto R., Bonaglia S., Li H., Hajati M.-C. and Li L. (2021) Submarine groundwater discharge impacts on coastal nutrient biogeochemistry. *Nat. Rev. Earth Environ.* **2**, 307–323.

Sauramo M. (1923) Studies on the Quaternary varve sediments in southern Finland. *Bulletin de la Commission géologique de Finlande* **60**, 1–164.

Sawicka J. E. and Brüchert V. (2017) Annual variability and regulation of methane and sulfate fluxes in Baltic Sea estuarine sediments. *Biogeosciences* **14**, 325–339.

Schaller S., Böttcher M. E., Buechi M. W., Epp L. S., Fabbri S. C., Gribenski N., Harms U., Krastel S., Liebezeit A., Lindhorst K., Marxen H., Raschke U., Schleheck D., Schmiedinger I., Schwalb A., Vogel H., Wessels M. and Anselmetti F. S. (2022) Postglacial evolution of Lake Constance: sedimentological and geochemical evidence from a deep-basin sediment core. *Swiss J. Geosci.* **115**. doi.10.1186/s00015-022-00412-1.

Schlüter M., Sauter E. J., Andersen C. E., Dahlgaard H. and Dando P. R. (2004) Spatial distribution and budget for submarine groundwater discharge in Eckernförde Bay (western Baltic Sea). *Limnol. Oceanogr.* **49**, 157–167.

Sinkko H., Hepolehto I., Lyra C., Rinta-Kanto J. M., Villnäs A., Norkko J., Norkko A. and Timonen S. (2019) Increasing oxygen deficiency changes rare and moderately abundant bacterial communities in coastal soft sediments. *Sci. Rep.*, 9.

Stahl D. A. and de la Torre J. R. (2012) Physiology and Diversity of Ammonia-Oxidizing Archaea. *Annu. Rev. Microbiol.* **66**, 83–101.

Stegen J. C., Fredrickson J. K., Wilkins M. J., Konopka A. E., Nelson W. C., Arntzen E. V., Chrisler W. B., Chu R. K., Danczak R. E., Fansler S. J., Kennedy D. W., Resch C. T. and Tfaily M. (2016) Groundwater–surface water mixing shifts ecological assembly processes and stimulates organic carbon turnover. *Nat. Commun.* **7**, 11237.

Szymczycha B., Vogler S. and Pempkowiak J. (2012) Nutrient fluxes via submarine groundwater discharge to the Bay of Puck, southern Baltic Sea. *Sci. Total Environ.* **438**, 86–93.

Thang N. M., Bruechert V., Formolo M., Wegener G., Ginters L., Jørgensen B. B. and Ferdelman T. G. (2013) The impact of sediment and carbon fluxes on the biogeochemistry of methane and sulfur in littoral Baltic Sea sediments (Himmerfjarden, Sweden). *Estuaries Coasts* **36**, 98–115.

Tolar B. B., Mosier A. C., Lund M. B. and Francis C. A. (2019). In *Nitrosarchaeum. Bergey's Manual of Systematics of Archaea and Bacteria*. Wiley, Hoboken, New Jersey, pp. 1–9.

Turner S., Pryer K. M., Miao V. P. W. and Palmer J. D. (1999) Investigating deep phylogenetic relationships among cyanobacteria and plastids by small subunit rRNA sequence analysis. In *Journal of Eukaryotic Microbiology Society of Protozoologists*, pp. 327–338.

Vallius H. (2014) Heavy metal concentrations in sediment cores from the northern Baltic Sea: declines over the last two decades. *Mar. Pollut. Bull.* **79**, 359–364.

Vanek V. and Lee D. R. (1991) Mapping submarine groundwater discharge areas - an example from Laholm Bay, southwest Sweden. *Limnol. Oceanogr.* **36**, 1250–1262.

Virtasalo, J.J., 2022. Multielement and grain-size data of short sediment cores from the Hanko submarine groundwater discharge site, northern Baltic Sea, Finland. *PANGAEA*, doi:10.1594/PANGAEA.942288.

Virtasalo, J.J., von Ahn, C., Jilbert, T., Bange, H.W., Jenner, A., Böttcher, M.E., Luoma, S., Lahaye, Y., 2022. Multielement, Cl^-, CH_4, NH_4, DIC concentrations and δ^2H, $\delta^{18}O$, δ^7Li, $\delta^{34}S$, $^{87}S/^{86}Sr$, $\delta^{13}C$-DIC composition of groundwater, seawater, and pockmark porewater from Hanko SGD site, Finland. *PANGAEA*, doi:10.1594/PANGAEA.942547.

Virtasalo J. J., Schröder J. F., Luoma S., Majaniemi J., Mursu J. and Scholten J. (2019) Submarine groundwater discharge site in the First Salpausselkä ice-marginal formation, south Finland. *Solid Earth* **10**, 405–423.

Virtasalo J. J., Ryabchuk D., Kotilainen A. T., Zhamoida V., Grigoriev A., Sivkov V. and Dorokhova E. (2014) Middle Holocene to present sedimentary environment in the easternmost Gulf of Finland (Baltic Sea) and the birth of the Neva River. *Mar. Geol.* **350**, 84–96.

von Ahn C. M. E., Scholten J. C., Malik C., Feldens P., Liu B., Dellwig O., Jenner A.-K., Papenmeier S., Schmiedinger I., Zeller M. A. and Böttcher M. E. (2021) A Multi-Tracer Study of Fresh Water Sources for a Temperate Urbanized Coastal Bay (Southern Baltic Sea). *Front. Environ. Sci.* **9**, 642346.

Wang Y. and Van Cappellen P. (1996) A multicomponent reactive transport model of early diagenesis?: Application to redox cycling in coastal marine sediments. *Geochim. Cosmochim. Acta* **60**, 2993–3014.

Werne J. P., Lyons T. W., Hollander D. J., Schouten S., Hopmans E. C. and Sinninge Damsté J. S. (2008) Investigating pathways of diagenetic organic matter sulfurization using compound-specific sulfur isotope analysis. *Geochim. Cosmochim. Acta* **72**, 3489–3502.

Westrich J. T. and Berner R. A. (1984) The role of sedimentary organic matter in bacterial sulfate reduction: The *G* model tested. *Limnol. Oceanogr.* **29**, 236–249.

Whiticar M. (1999) Carbon and hydrogen isotope systematics of bacterial formation and oxidation of methane. *Chem. Geol.* **161**, 291–314.

Whiticar M. J. (2002) Diagenetic relationship of methanogenesis, nutrients, acoustic turbidity, pockmarks and freshwater seepages in Eckernförde Bay. *Mar. Geol.* **182**, 29–53.

Whiticar M. J. and Werner F. (1981) Pockmarks: submarine vents of natural gas or freshwater seeps. *Geo-Mar. Lett.* **1**, 193–199.

Wiesenburg D. and Guinasso N. (1979) Equilibrium solubilities of methane, carbon-monoxide, and hydrogen in water and sea-water. *J. Chem. Eng. Data* **24**, 356–360.

Winde V., Böttcher M. E., Escher P., Böning P., Beck M., Liebezeit G. and Schneider B. (2014) Tidal and spatial variations of DI13C and aquatic chemistry in a temperate tidal basin during winter time. *J. Mar. Syst.* **129**, 394–402.

Wolski T., Wiśniewski B., Giza A., Kowalewska-Kalkowska H., Boman H., Grabbi-Kaiv S., Hammarklint T., Holfort J. and Lydeikaite Z. (2014) Extreme sea levels at selected stations on the Baltic Sea coast. *Oceanologia* **56**, 259–290.

Wu Z., Liu B., Escher P., Kowalski N. and Böttcher M. E. (2018) Carbon diagenesis in different sedimentary environments of the subtropical Beibu Gulf, South China Sea. *J. Mar. Sys.* **186**, 68–84.

Zhou Y. Q., Sawyer A. H., David C. H. and Famiglietti J. S. (2019) Fresh submarine groundwater discharge to the near-global coast. *Geophys. Res. Lett.* **46**, 5855–5863.

Associate editor: Filip Meysman